MVP: MULTIVARIATE POLYNOMIALS FOR CONDITIONAL DATA GENERATION

Anonymous authors
Paper under double-blind review

ABSTRACT

Conditional Generative Adversarial Nets (cGANs) have been widely adopted for image generation. cGANs take i) a noise vector and ii) a conditional variable as input. The conditional variable can be discrete (e.g., a class label) or continuous (e.g., an input image) resulting into class-conditional (image) generation and image-to-image translation models, respectively. However, depending on whether the conditional variable is discrete or continuous, various cGANs employ substantially different deep architectures and loss functions for their training. In this paper, we propose a novel framework, called *MVP*, for conditional data generation. MVP resorts to multivariate polynomials of higher-order and treats in a unified way both discrete and continuous conditional variables. MVP is highly expressive, capturing higher-order auto- and cross-correlations of input variables (noise vector and conditional variable). Tailored sharing schemes are designed between the polynomial's parameter tensors, which result in simple recursive formulas. MVP can synthesize realistic images in both class-conditional and image-to-image translation tasks even in the absence of activation functions between the layers.

1 INTRODUCTION

Modelling high-dimensional distributions and generating samples from complex distributions are fundamental tasks in machine learning. Generative adversarial networks (GANs) (Goodfellow et al., 2014) have demonstrated spectacular results in the two tasks using both unsupervised (Miyato et al., 2018) and supervised (Brock et al., 2019) learning. In the unsupervised setting, (the generator of) a GAN accepts as input a noise vector $\boldsymbol{z}_{\mathrm{I}}$ and maps the noise vector to a high-dimensional output. The supervised models, called conditional Generative Adversarial Nets (cGANs) (Mirza & Osindero, 2014), accept both a noise vector $\boldsymbol{z}_{\mathrm{I}}$ and an additional conditional variable $\boldsymbol{z}_{\mathrm{II}}$ that facilitates the generation. The conditional variable can be discrete (e.g., a class or an attribute label) or continuous (e.g., a low-resolution image). The impressive results obtained with both discrete conditional input (Brock et al., 2019) and continuous conditional input (Park et al., 2019; Ledig et al., 2017) have led to a plethora of applications that range from text-to-image synthesis (Qiao et al., 2019) to deblurring (Yan & Wang, 2017) and medical analysis (You et al., 2019).

Despite the similarity in the formulation for discrete and continuous conditional input (i.e., learning the function $G(\boldsymbol{z}_{\mathrm{I}}, \boldsymbol{z}_{\mathrm{II}})$), the literature has focused on substantially different architectures and losses. Frequently, techniques are simultaneously developed, e.g., the self-attention in the class-conditional Self-Attention GAN (Zhang et al., 2019) and in the Attention-GAN (Chen et al., 2018) with continuous conditional input. This delays the progress since practitioners develop twice as many architectures and losses for every case. A couple of straightforward ideas can be employed to unify the behavior of the two conditional variable types. One idea is to use an encoder network to obtain representations that are independent of the conditional variable. This has two drawbacks: i) the network ignores the noise and a deterministic one-variable mapping is learned (Isola et al., 2017), ii) such encoder has not been successful so far for discrete conditional input. An alternative idea is to directly concatenate the labels in the latent space instead of finding an embedding. In AC-GAN (Odena et al., 2017) the class labels are concatenated with the noise; however, the model does not scale well beyond 10 classes. We argue that concatenation of the input is only capturing additive correlation and not higher-order interactions between the inputs. A detailed discussion is conducted on sec. D (in the Appendix).

A polynomial expansion with respect to the input variables can capture such higher-order correlations. Π-Net (Chrysos et al., 2020) casts the function approximation into a polynomial expansion of a single input variable. By concatenating the input variables, we can express the function approximation as a polynomial of the fused variable. However, the concatenation reduces the flexibility of the model significantly, e.g., it enforces the same order of expansion with respect to the different variables and it only allows the same parameter sharing scheme to all variables.

We introduce a multivariate framework, called *MVP*, for conditional data generation. MVP resorts to multivariate polynomials with two input variables, i.e., $\boldsymbol{z}_{\mathrm{I}}$ for the noise vector and $\boldsymbol{z}_{\mathrm{II}}$ for the conditional variable. MVP captures higher-order auto- and cross-correlations between the variables. By imposing a tailored structure in the higher-order interactions, we obtain an intuitive, recursive formulation for MVP. The formulation is flexible and enables different constraints to be applied to each variable and its associated parameters. The formulation can be trivially extended to M input variables. In summary, our contributions are the following:

- We introduce a framework, called MVP, that expresses a high-order, multivariate polynomial for conditional data generation. Importantly, MVP treats both discrete and continuous conditional variables in a unified way.
- MVP is trained on four different datasets for both class-conditional generation and image-to-image translation tasks. The trained models rely on both input variables, i.e., they do not ignore the noise vector.
- To illustrate the expressivity of the model, we also experiment with generators that do not use activation functions between the layers. We verify that MVP can synthesize realistic images even in the absence of activation functions between the layers.

The source code of MVP will be published upon the acceptance of the paper.

2 Related work

The literature on conditional data generation is vast; dedicated surveys per task (Agnese et al., 2019; Wu et al., 2017b) can be found for the interested reader. Below, we review representative works in conditional generation and then we summarize the recent progress in multiplicative interactions.

2.1 Conditional generative models

The challenging nature of image/video generation has led to a proliferation of conditional models. Although cGAN (Mirza & Osindero, 2014) is a general framework, since then the methods developed for conditional generation differ substantially depending on the type of conditional data. We present below representative works of the two categories, i.e., discrete and continuous conditional data, and their combination.

Discrete conditional variable: This is most frequently used for class-conditional generation (Miyato et al., 2018; Brock et al., 2019; Kaneko et al., 2019). Conditional normalization (Dumoulin et al., 2017; De Vries et al., 2017) techniques have been popular in the case of discrete conditional input, e.g., in generation of natural scenes images (Miyato et al., 2018; Brock et al., 2019). Conditional normalization assigns different statistics per class, which might be an obstacle to generalization of the method to unseen classes (Zhao et al., 2018). In AC-GAN (Odena et al., 2017), they concatenate the class labels with the noise; however, their model does not scale well (i.e., they train one model per 10 classes). The aforementioned methods cannot be trivially used or modified for continuous conditional input. Text-to-image generation models (Qiao et al., 2019; Li et al., 2019; Zhang et al., 2018; Xu et al., 2018) use a specialized branch to embed the text labels.

Continuous conditional variable: The influential work of pix2pix (Isola et al., 2017) has become the reference point for continuous conditional input. The conditional input is embedded in a low-dimensional space (with an encoder), and then mapped to a high-dimensional output (through a decoder). The framework has been widely used for inverse tasks (Ledig et al., 2017; Pathak et al., 2016; Wu et al., 2017a; Yu et al., 2018a; Grm et al., 2019; Xie et al., 2018; Yan & Wang, 2017), conditional pose generation (Ma et al., 2017; Siarohin et al., 2018; Liang et al., 2019), representation learning (Tran et al., 2017), conditional video generation (Wang et al., 2018a), generation from

semantic labels (Wang et al., 2018b), image blending (Wu et al., 2019; Zhan et al., 2019). We recognize two major drawbacks in the aforementioned methods: a) they cannot be easily adapted for discrete conditional input, b) they learn a deterministic mapping, i.e., the noise is typically ignored. However, in many real applications, such as inverse tasks, the mapping is not one-to-one; there are multiple plausible outputs for every conditional input. The auxiliary losses used in such works, e.g., ℓ_1 loss (Isola et al., 2017), perceptual loss (Ledig et al., 2017), are an additional drawback. Those losses both add hyper-parameters that require tuning and are domain-specific, thus it is challenging to transfer them to different domains or even different datasets. On the contrary, in our experiments, we do not use any additional loss.

Discrete and continuous conditional variables: Few works combine both discrete and continuous conditional inputs (Yu et al., 2018b; Xu et al., 2017; Lu et al., 2018). However, these methods include significant engineering (e.g., multiple discriminators (Xu et al., 2017), auxiliary losses), while often the generator learns to ignore the noise (similarly to the continuous conditional input).

The idea of Li et al. (2020) is most closely related to our work. They introduce a unifying framework for paired (Isola et al., 2017) and unpaired (Zhu et al., 2017) learning. However, their framework assumes a continuous conditional input, while ours can handle discrete conditional input (e.g., class labels). In addition, their method requires a pre-trained teacher generator, while ours consists of a single generator trained end-to-end.

2.2 Multiplicative interactions

Multiplicative connections have long been adopted in computer vision and machine learning (Shin & Ghosh, 1991; Hochreiter & Schmidhuber, 1997; Bahdanau et al., 2015). The idea is to combine the inputs through elementwise products or other diagonal forms. Even though multiplicative connections have successfully been applied to different tasks, until recently there was no comprehensive study of their expressivity versus the standard feedforward networks. Jayakumar et al. (2020) include the proof that second order multiplicative operators can represent a greater class of functions than classic feed-forward networks. Even though we capitalize on the theoretical argument, our framework can express any higher-order interactions while the framework of Jayakumar et al. (2020) is limited to second order interactions.

Higher-order interactions have been studied in the tensor-related literature (Kolda & Bader, 2009; Debals & De Lathauwer, 2017). However, their adaptation in modern deep architectures has been slower. Chrysos et al. (2020) propose high-order polynomial for mapping the input $\boldsymbol{z}$ to the output $\boldsymbol{x} = G(\boldsymbol{z})$. Their framework is limited to a single input variable and cannot handle the multivariate cases that are the focus of this work. SPADE (Park et al., 2019) can be interpreted as a polynomial expansion with respect to the conditional variable, i.e., a semantic layout in their case. Capturing higher-order correlations with respect to one of the variables (and not the rest) restricts the expressivity of the model. Further differences of MVP from Chrysos et al. (2020) and Park et al. (2019) are deferred to sec. E and sec. F respectively.

3 Method

The framework for a multivariate polynomial with a two-variable input is introduced (sec. 3.1). The derivation, further intuition and additional models are deferred to the Appendix (sec. B). The crucial technical details, including the stability of the polynomial, are developed in sec. 3.2. We emphasize that a multivariate polynomial can approximate any function (Stone, 1948; Nikol'skii, 2013), i.e., a multivariate polynomial is a universal approximator.

Table 1: Symbols

Symbol	Role
N	Expansion order of the polynomial
k	Rank of the decompositions
$\boldsymbol{z}_{\text{I}}, \boldsymbol{z}_{\text{II}}$	Inputs to the polynomial
n, ρ	Auxiliary variables
$\boldsymbol{\mathcal{W}}^{[n,\rho]}$	Parameter tensor of the polynomial
$\boldsymbol{U}_{[n]}, \boldsymbol{C}, \boldsymbol{\beta}$	Learnable parameters
$*$	Hadamard product

Notation:Tensors/matrices/vectors are symbolized by calligraphic/uppercase/lowercase boldface letters e.g., $\boldsymbol{\mathcal{W}}$,$\boldsymbol{W}$,$\boldsymbol{w}$. The *mode-m vector product* of $\boldsymbol{\mathcal{W}}$ (of order M) with a vector $\boldsymbol{u} \in \mathbb{R}^{I_m}$ is $\boldsymbol{\mathcal{W}} \times_m \boldsymbol{u}$ and results in a tensor of order $M-1$. We assume that $\prod_{i=a}^{b} x_i = 1$ when $a > b$. The core symbols are summarized in Table 1, while a detailed tensor notation is deferred to the Appendix (sec. B.1).

3.1 TWO INPUT VARIABLES

Given two input variables [1] $\boldsymbol{z}_{\text{I}}, \boldsymbol{z}_{\text{II}} \in \mathbb{K}^d$ where $\mathbb{K} \subseteq \mathbb{R}$ or $\mathbb{K} \subseteq \mathbb{N}$, the goal is to learn a function $G : \mathbb{K}^{d \times d} \rightarrow \mathbb{R}^o$ that captures the higher-degree interactions between the elements of the two inputs. We can learn such higher-degree interactions as polynomials of two input variables. A polynomial of expansion order $N \in \mathbb{N}$ with output $\boldsymbol{x} \in \mathbb{R}^o$ has the form:

$$\boldsymbol{x} = G(\boldsymbol{z}_{\text{I}}, \boldsymbol{z}_{\text{II}}) = \sum_{n=1}^{N} \sum_{\rho=1}^{n+1} \left(\boldsymbol{\mathcal{W}}^{[n,\rho]} \prod_{j=2}^{\rho} \times_j \boldsymbol{z}_{\text{I}} \prod_{\tau=\rho+1}^{n+1} \times_\tau \boldsymbol{z}_{\text{II}} \right) + \boldsymbol{\beta} \tag{1}$$

where $\boldsymbol{\beta} \in \mathbb{R}^o$ and $\boldsymbol{\mathcal{W}}^{[n,\rho]} \in \mathbb{R}^{o \times \prod_{m=1}^{n} \times_m d}$ for $n \in [1, N], \rho \in [1, n+1]$ are the learnable parameters. The expansion depends on two (independent) variables, hence we use the n and ρ as auxiliary variables. The two products of (1) do not overlap, i.e., the first multiplies the modes $[2, \rho]$ (of $\boldsymbol{\mathcal{W}}^{[n,\rho]}$) with $\boldsymbol{z}_{\text{I}}$ and the other multiplies the modes $[\rho+1, n+1]$ with $\boldsymbol{z}_{\text{II}}$.

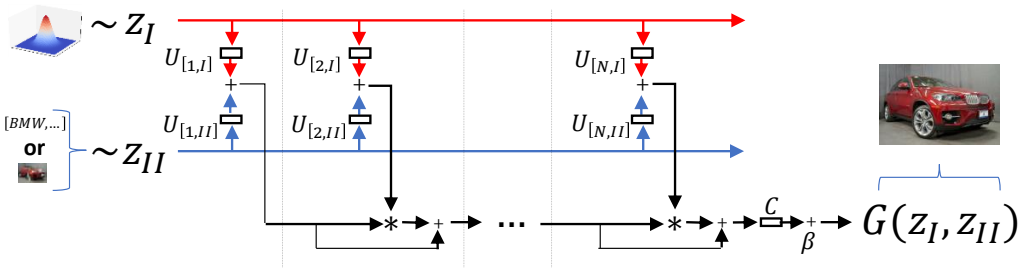

Figure 1: Abstract schematic for N^{th} order approximation of $\boldsymbol{x} = G(\boldsymbol{z}_I, \boldsymbol{z}_{II})$. The inputs $\boldsymbol{z}_I, \boldsymbol{z}_{II}$ are symmetric in our formulation. We denote with $\boldsymbol{z}_I$ a sample from a prior distribution (e.g., Gaussian), while $\boldsymbol{z}_{II}$ symbolizes a sample from a conditional input (e.g., class label or low-resolution image).

Recursive relationship: The aforementioned derivation can be generalized to an arbitrary expansion order. The recursive formula for an arbitrary order $N \in \mathbb{N}$ is the following:

$$\boldsymbol{x}_n = \boldsymbol{x}_{n-1} + \left(\boldsymbol{U}_{[n,I]}^T \boldsymbol{z}_{\text{I}} + \boldsymbol{U}_{[n,II]}^T \boldsymbol{z}_{\text{II}} \right) * \boldsymbol{x}_{n-1} \tag{2}$$

for $n = 2, \ldots, N$ with $\boldsymbol{x}_1 = \boldsymbol{U}_{[1,I]}^T \boldsymbol{z}_{\text{I}} + \boldsymbol{U}_{[1,II]}^T \boldsymbol{z}_{\text{II}}$ and $\boldsymbol{x} = \boldsymbol{C}\boldsymbol{x}_N + \boldsymbol{\beta}$. The parameters $\boldsymbol{C} \in \mathbb{R}^{o \times k}, \boldsymbol{U}_{[n,\phi]} \in \mathbb{R}^{d \times k}$ for $n = 1, \ldots, N$ and $\phi = \{I, II\}$ are learnable.

The intuition behind this model is the following: An embedding is initially found for each of the two input variables, then the two embeddings are added together and they are multiplied elementwise with the previous approximation. The different embeddings for each of the input variables allows us to implement $\boldsymbol{U}_{[n,I]}$ and $\boldsymbol{U}_{[n,II]}$ with different constraints, e.g., $\boldsymbol{U}_{[n,I]}$ to be a dense layer and $\boldsymbol{U}_{[n,II]}$ to be a convolution.

3.2 MODEL EXTENSIONS AND TECHNICAL DETAILS

There are three limitations in (2). Those are the following: a) (2) describes a polynomial expansion of a two-variable input, b) each expansion order requires additional layers, c) high-order polynomials might suffer from unbounded values. Those limitations are addressed below.

Our model can be readily extended beyond two-variable input; an extension with three-variable input is developed in sec. C. The pattern (for each order) is similar to the two-variable input: a) a different embedding is found for each input variable, b) the embeddings are added together, c) the result is multiplied elementwise with the representation of the previous order.

The polynomial expansion of (2) requires $\Theta(N)$ layers for an Nth order expansion. That is, each new order n of expansion requires new parameters $\boldsymbol{U}_{[n,I]}$ and $\boldsymbol{U}_{[n,II]}$. However, the order of expansion

[1] To avoid cluttering the notation we use same dimensionality for the two inputs. However, the derivations apply for different dimensionalities, only the dimensionality of the tensors change slightly.

can be increased without increasing the parameters substantially. To that end, we can capitalize on the product of polynomials. Specifically, let N_1 be the order of expansion of the first polynomial. The output of the first polynomial is fed into a second polynomial, which has expansion order of N_2. Then, the output of the second polynomial will have an expansion order of $N_1 \cdot N_2$. The product of polynomials can be used with arbitrary number of polynomials; it suffices the output of the τth polynomial to be the input to the $(\tau+1)^{th}$ polynomial. For instance, if we assume a product of $\Phi \in \mathbb{N}$ polynomials, where each polynomial has an expansion order of two, then the polynomial expansion is of 2^{Φ} order. In other words, we need $\Theta(\log_2(N))$ layers to achieve an Nth order expansion.

In algebra, higher-order polynomials are unbounded and can thus suffer from instability for large values. To avoid such instability, we take the following three steps: a) MVP samples the noise vector from the uniform distribution, i.e., from the bounded interval of $[-1, 1]$, b) a hyperbolic tangent is used in the output of the generator as a normalization, i.e., it constrains the outputs in the bounded interval of $[-1, 1]$, c) batch normalization (Ioffe & Szegedy, 2015) is used to convert the representations to zero-mean. We emphasize that in GANs the hyperbolic tangent is the default activation function in the output of the generator, hence it is not an additional requirement of our method. Additionally, in our preliminary experiments, the uniform distribution can be changed for a Gaussian distribution without any instability. A theoretical analysis on the bounds of such multivariate polynomials would be an interesting subject for future work.

4 EXPERIMENTS

The proposed MVP is empirically evaluated in three settings: a) a class-conditional generation, i.e., with discrete conditional input, b) an image-to-image translation, i.e., with continuous conditional input, c) a mixed conditional setting with two conditional variables. The goal is to showcase how MVP can be used with both discrete and continuous conditional inputs. Even though architectures specialized for a single task (e.g., Ledig et al. (2017)) perform well in that task, their well-selected inductive biases (e.g., perceptual or ℓ_1 loss) do not generalize well in other domains or different conditional inputs. Hence, our goal is not to demonstrate state-of-the-art results in specific tasks, but rather to propose one generic formulation. Further experiments (e.g., class-conditional generation with SVHN or MNIST to SVHN translation; sec H), the details on the datasets and the evaluation metrics (sec. G) are deferred to the Appendix. Throughout the experimental section, we reserve the symbol $\boldsymbol{z}_{\Pi}$ for the conditional input (e.g., a class label).

Our framework, e.g., (2), does not include any activation functions. To verify the expressivity of our framework, we maintain the same setting for the majority of the experiments below. Particularly, the generator does not have activation functions between the layers; there is only a hyperbolic tangent in the output space for normalization. Training a generator without activation functions between the layers also emerged in Π-Net (Chrysos et al., 2020), where the authors demonstrate the challenges in such framework. However, we conduct one experiment using a strong baseline with activation functions. That is, a comparison with SNGAN (Miyato & Koyama, 2018) in class-conditional generation is performed (sec. 4.1).

Baselines: 'Π-Net-SICONC' implements a polynomial expansion of a single variable, i.e., by concatenating all the input variables. 'SPADE' implements a polynomial expansion with respect to the conditional variable. Also, 'GAN-CONC' and 'GAN-ADD' are added as baselines, where we replace the Hadamard products with concatenation and addition respectively. An abstract schematic of the differences between the compared polynomial methods is depicted in Fig. 7, while a detailed description of all methods is deferred to sec. G. Each experiment is conducted **five** times and the mean and the standard deviation are reported.

4.1 CLASS-CONDITIONAL GENERATION

The first experiment is on class-conditional generation, where the conditional input is a class label in the form of one-hot vector. Two types of networks are utilized: a) a resnet-based generator (SNGAN), b) a polynomial generator (Π-Net) based on Chrysos et al. (2020). The former network has exhibited strong performance the last few years, while the latter bears resemblance to the formulation we propose in this work.

Table 2: Quantitative evaluation on class-conditional generation with resnet-based generator (i.e., SNGAN). Higher Inception Score (IS) (Salimans et al., 2016) (lower Frechet Inception Distance (FID) (Heusel et al., 2017)) indicates better performance. The baselines improve the IS of SNGAN, however they cannot improve the FID. Nevertheless, SNGAN-MVP improves upon all the baselines in both the IS and the FID.

class-conditional generation on CIFAR10		
Model	IS (↑)	FID (↓)
SNGAN	8.30 ± 0.11	14.70 ± 0.97
SNGAN-CONC	8.50 ± 0.49	30.65 ± 3.55
SNGAN-ADD	8.65 ± 0.11	15.47 ± 0.74
SNGAN-SPADE	8.69 ± 0.19	21.74 ± 0.73
SNGAN-MVP	$\mathbf{8.77 \pm 0.12}$	$\mathbf{14.22 \pm 0.66}$

Resnet-based generator: The experiment is conducted by augmenting the resnet-based generator of SNGAN. The quantitative results are in Table 2 and synthesized samples are illustrated in Fig. 2(a). SNGAN-MVP improves upon all the baselines in both the Inception score (IS) (Salimans et al., 2016) and the FID (Heusel et al., 2017). The proposed formulation enables inter-class interpolations. That is, the noise $\boldsymbol{z}_{\mathrm{I}}$ is fixed, while the class $\boldsymbol{z}_{\mathrm{II}}$ is interpolated. Even though inter-class interpolations have been performed in datasets with thousands of classes (Brock et al., 2019), inter-class interpolations in CIFAR10 have not emerged. In Fig. 2(b) and Fig. 2(c), intra-class and inter-class linear interpolations are illustrated respectively. Both the quantitative and the qualitative results exhibit the effectiveness of our framework.

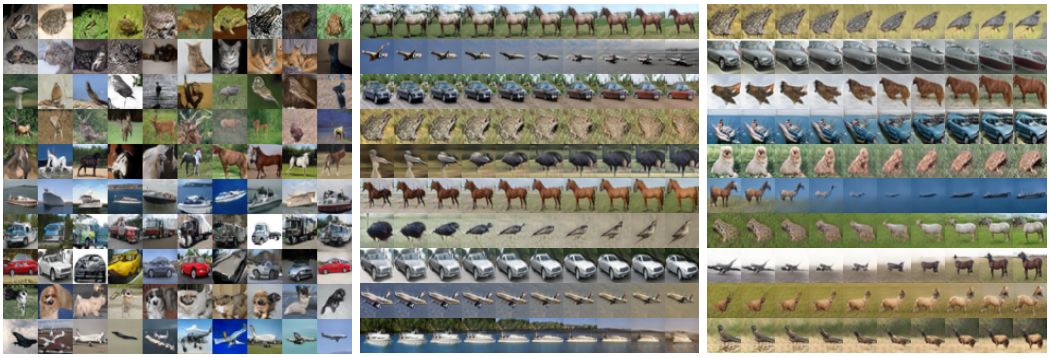

(a) Random samples per class (b) Intra-class interpolation (c) Inter-class interpolation

Figure 2: Synthesized images by MVP in the class-conditional CIFAR10 (with resnet-based generator): (a) Random samples where each row depicts the same class, (b) Intra-class linear interpolation from a source to the target, (c) inter-class linear interpolation. In inter-class interpolation, the class labels of the leftmost and rightmost images are one-hot vectors, while the rest are interpolated in-between; the resulting images are visualized. In all three cases, MVP synthesizes realistic images.

Π-Net-based generator: A product of polynomials, based on Π-Net, is selected as the baseline architecture for the generator. Π-Net has conditional batch normalization (CBN) in the generator, while in the rest compared methods CBN is replaced by batch normalization. The results in CIFAR10 are summarized in Table 3 (left), where MVP outperforms all the baselines by a large margin. An additional experiment is performed in Cars196 that has 196 classes. The results in Table 3 (right) depict a substantial improvement over the all the baselines (53.9% reduction over the best-performing baseline). We should note that the baseline was not built for conditional generation, however we have done our best effort to optimize the respective hyper-parameters. We hypothesize that the improvement arises because of the correlations of the classes. That is, the 196 classes might be correlated (e.g., the SUV cars of different carmakers share several patterns). Such correlations are captured by our framework, while they might be missed when learning different normalization statistics per class. Overall, MVP synthesizes plausible images (Fig. 3) even in the absence of activation functions.

Table 3: Quantitative evaluation on class-conditional generation with Π-Net-based generator. In CIFAR10, there is a considerable improvement on the IS, while in Cars196 FID drops dramatically with MVP. We hypothesize that the dramatic improvement in Cars196 arises because of the correlations of the classes. For instance, the SUV cars (of different carmakers) share several patterns, which are captured by our high-order interactions, while they might be missed when learning different normalization statistics per class.

class-conditional generation on CIFAR10		
Model	IS (↑)	FID (↓)
GAN-CONC	3.73 ± 0.32	294.33 ± 8.16
GAN-ADD	3.74 ± 0.60	298.53 ± 16.54
SPADE	4.00 ± 0.53	294.21 ± 16.33
Π-Net-SICONC	6.65 ± 0.60	71.81 ± 33.00
Π-Net	7.54 ± 0.16	37.26 ± 1.86
MVP	$\mathbf{7.87 \pm 0.21}$	$\mathbf{34.35 \pm 2.68}$

class-conditional generation on Cars196	
Model	FID (↓)
GAN-CONC	240.45 ± 16.79
GAN-ADD	208.72 ± 12.65
SPADE	168.19 ± 39.71
Π-Net-SICONC	153.39 ± 27.93
Π-Net	120.40 ± 28.65
MVP	$\mathbf{55.48 \pm 3.16}$

(a) Class-conditional generation (b) Class-conditional generation (c) Block-inpainting

Figure 3: Synthesized images by MVP in the (a), (b) class-conditional generation (sec. 4.1) and (b) block-inpainting (sec. 4.2). The networks do not include activation functions between the layers. In class-conditional generation, each row depicts a single class. Notice how the MVP synthesizes diverse images even in the absence of activation functions.

4.2 Continuous conditional input

The performance of MVP is scrutinized in tasks with continuous conditional input, e.g., super-resolution. The conditional input $\boldsymbol{z}_{\Pi}$ is an input image, e.g., a low-resolution sample or a corrupted sample. Even though the core architecture remains the same, a single change is made in the structure of the discriminator: Motivated by (Miyato & Koyama, 2018), we include an elementwise product of $\boldsymbol{z}_{\Pi}$ with the real/fake image in the discriminator. This stabilizes the training and improves the results. A wealth of literature is available on such continuous conditional inputs (sec. 2.1), however we select the challenging setting of using a generator without activation functions between the layers.

Table 4: Quantitative evaluation on super-resolution with Π-Net-based generator on Cars196. The task on the left is super-resolution $16\times$, while on the right the task is super-resolution $8\times$. Our variant of SPADE, i.e., SPADE-MVP (details in sec. G), vastly improves the original SPADE. The full two-variable model, i.e., MVP, outperforms the compared methods.

Super-resolution $16\times$ Cars196	
Model	FID (↓)
SPADE	111.75 ± 13.41
Π-Net-SICONC	80.16 ± 12.42
SPADE-MVP	72.63 ± 3.18
MVP	$\mathbf{60.42 \pm 6.19}$

Super-resolution $8\times$ Cars196	
Model	FID (↓)
SPADE	119.18 ± 14.82
Π-Net-SICONC	186.42 ± 40.84
SPADE-MVP	64.76 ± 8.26
MVP	$\mathbf{62.76 \pm 4.37}$

The experiments are performed in (a) super-resolution, (b) block-inpainting. Super-resolution assumes a low-resolution image is available, while in block inpainting, a (rectangular) part of the image is

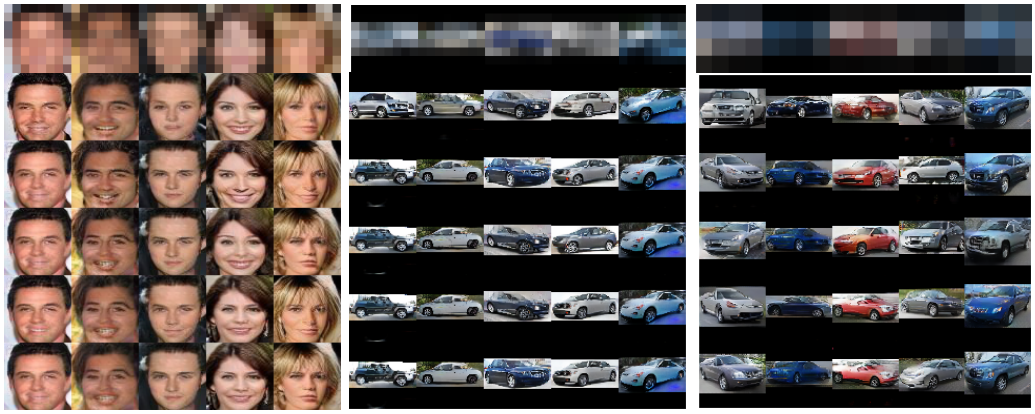

(a) Super-resolution $8\times$ (b) Super-resolution $8\times$ (c) Super-resolution $16\times$

Figure 4: Synthesized images for super-resolution by (a), (b) $8\times$, (c) $16\times$. The first row depicts the conditional input (i.e., low-resolution image). The rows 2-6 depict outputs of the MVP when a noise vector is sampled per row. Notice how the noise changes (a) the smile or the pose of the head, (b) the color, car type or even the background, (c) the position of the car.

missing. The two tasks belong in the broader category of 'inverse tasks', and they are significant both for academic reasons but also for commercial reasons (Sood et al., 2018; You et al., 2019). Such inverse tasks are underdetermined; each input image corresponds to several plausible output images.

The FID scores in Cars196 for the task of super-resolution are reported in Table 4. In super-resolution $16\times$, $\boldsymbol{z}_{\text{II}}$ has 48 dimensions, while in super-resolution $8\times$, $\boldsymbol{z}_{\text{II}}$ has 192 dimensions. Notice that the performance of Π-Net-SICONC deteriorates substantially when the dimensionality of the conditional variable increases. That validates our intuition about the concatenation in the input of the generator (sec. E). We also report the SPADE-MVP, which captures higher-order correlations with respect to the first variable as well (further details in sec. G). The proposed SPADE-MVP outperforms the original SPADE, however it cannot outperform the full two-variable model, i.e., MVP. MVP maintains outperforms all baselines by a large margin.

The qualitative results on (a) super-resolution $8\times$ on CelebA, (b) super-resolution $8\times$ on Cars196, (c) super-resolution $16\times$ on Cars196 are illustrated in Fig. 4. Similarly the qualitative results on block-inpainting are visualized in Fig. 3. For each conditional image, different noise vectors $\boldsymbol{z}_{\text{I}}$ are sampled. Notice that the corresponding synthesized images differ in the fine-details. For instance, changes in the mouth region, the car type or position and even background changes are observed. Thus, MVP results in high-resolution images that i) correspond to the conditional input, ii) vary in fine-details. Similar variation has emerged even when the source and the target domains differ substantially, e.g., in the translation of MNIST digits to SVHN digits (sec. H.3).

5 Conclusion

The topic of conditional data generation is the focus of this work. A multivariate polynomial model, called MVP, is introduced. MVP approximates a function $G(\boldsymbol{z}_{\text{I}}, \boldsymbol{z}_{\text{II}})$ with inputs $\boldsymbol{z}_{\text{I}}$ (e.g., sample from a Gaussian distribution) and $\boldsymbol{z}_{\text{II}}$ (e.g., class or low-resolution image). MVP resorts to multivariate polynomials with arbitrary conditional inputs, which capture high-order correlations of the inputs. The empirical evaluation confirms that our framework can synthesize realistic images in both class-conditional generation (trained on CIFAR10 and Cars196), and image-to-image translation (both super-resolution and block-inpainting). We also showcase that it can be extended to three-variable input with class-conditional super-resolution. In addition to conditional data generation, the proposed framework can be used in tasks requiring fusion of different types of variables.

REFERENCES

Jorge Agnese, Jonathan Herrera, Haicheng Tao, and Xingquan Zhu. A survey and taxonomy of adversarial neural networks for text-to-image synthesis. *arXiv preprint arXiv:1910.09399*, 2019.

Dzmitry Bahdanau, Kyunghyun Cho, and Yoshua Bengio. Neural machine translation by jointly learning to align and translate. In *International Conference on Learning Representations (ICLR)*, 2015.

Andrew Brock, Jeff Donahue, and Karen Simonyan. Large scale gan training for high fidelity natural image synthesis. In *International Conference on Learning Representations (ICLR)*, 2019.

Xinyuan Chen, Chang Xu, Xiaokang Yang, and Dacheng Tao. Attention-gan for object transfiguration in wild images. In *European Conference on Computer Vision (ECCV)*, pp. 164–180, 2018.

Grigorios Chrysos, Stylianos Moschoglou, Yannis Panagakis, and Stefanos Zafeiriou. Polygan: High-order polynomial generators. *arXiv preprint arXiv:1908.06571*, 2019.

Grigorios Chrysos, Stylianos Moschoglou, Giorgos Bouritsas, Yannis Panagakis, Jiankang Deng, and Stefanos Zafeiriou. $\pi-$nets: Deep polynomial neural networks. In *Conference on Computer Vision and Pattern Recognition (CVPR)*, 2020.

Antonia Creswell, Tom White, Vincent Dumoulin, Kai Arulkumaran, Biswa Sengupta, and Anil A Bharath. Generative adversarial networks: An overview. *IEEE Signal Processing Magazine*, 35(1): 53–65, 2018.

Harm De Vries, Florian Strub, Jérémie Mary, Hugo Larochelle, Olivier Pietquin, and Aaron C Courville. Modulating early visual processing by language. In *Advances in neural information processing systems (NeurIPS)*, pp. 6594–6604, 2017.

O Debals and L De Lathauwer. The concept of tensorization. Technical report, Technical Report 17–99, ESAT–STADIUS, KU Leuven, Belgium, 2017.

Vincent Dumoulin, Jonathon Shlens, and Manjunath Kudlur. A learned representation for artistic style. 2017.

Ian Goodfellow, Jean Pouget-Abadie, Mehdi Mirza, Bing Xu, David Warde-Farley, Sherjil Ozair, Aaron Courville, and Yoshua Bengio. Generative adversarial nets. In *Advances in neural information processing systems (NeurIPS)*, 2014.

Klemen Grm, Walter J Scheirer, and Vitomir Štruc. Face hallucination using cascaded super-resolution and identity priors. *IEEE Transactions in Image Processing (TIP)*, 29(1):2150–2165, 2019.

Martin Heusel, Hubert Ramsauer, Thomas Unterthiner, Bernhard Nessler, and Sepp Hochreiter. Gans trained by a two time-scale update rule converge to a local nash equilibrium. In *Advances in neural information processing systems (NeurIPS)*, pp. 6626–6637, 2017.

Sepp Hochreiter and Jürgen Schmidhuber. Long short-term memory. *Neural computation*, 9(8): 1735–1780, 1997.

Sergey Ioffe and Christian Szegedy. Batch normalization: Accelerating deep network training by reducing internal covariate shift. In *International Conference on Machine Learning (ICML)*, 2015.

Phillip Isola, Jun-Yan Zhu, Tinghui Zhou, and Alexei A Efros. Image-to-image translation with conditional adversarial networks. In *Conference on Computer Vision and Pattern Recognition (CVPR)*, 2017.

Siddhant M. Jayakumar, Wojciech M. Czarnecki, Jacob Menick, Jonathan Schwarz, Jack Rae, Simon Osindero, Yee Whye Teh, Tim Harley, and Razvan Pascanu. Multiplicative interactions and where to find them. In *International Conference on Learning Representations (ICLR)*, 2020.

Takuhiro Kaneko, Yoshitaka Ushiku, and Tatsuya Harada. Label-noise robust generative adversarial networks. In *Conference on Computer Vision and Pattern Recognition (CVPR)*, pp. 2467–2476, 2019.

Tero Karras, Samuli Laine, and Timo Aila. A style-based generator architecture for generative adversarial networks. In *Conference on Computer Vision and Pattern Recognition (CVPR)*, 2019.

Tamara G Kolda and Brett W Bader. Tensor decompositions and applications. *SIAM review*, 51(3): 455–500, 2009.

Jonathan Krause, Michael Stark, Jia Deng, and Li Fei-Fei. 3d object representations for fine-grained categorization. In *Conference on Computer Vision and Pattern Recognition Workshops (CVPR'W)*, pp. 554–561, 2013.

Alex Krizhevsky, Vinod Nair, and Geoffrey Hinton. The cifar-10 dataset. *online: http://www. cs. toronto. edu/kriz/cifar. html*, 55, 2014.

Yann LeCun, Léon Bottou, Yoshua Bengio, Patrick Haffner, et al. Gradient-based learning applied to document recognition. *Proceedings of the IEEE*, 86(11):2278–2324, 1998.

Christian Ledig, Lucas Theis, Ferenc Huszár, Jose Caballero, Andrew Cunningham, Alejandro Acosta, Andrew Aitken, Alykhan Tejani, Johannes Totz, Zehan Wang, et al. Photo-realistic single image super-resolution using a generative adversarial network. In *Conference on Computer Vision and Pattern Recognition (CVPR)*, 2017.

Bowen Li, Xiaojuan Qi, Thomas Lukasiewicz, and Philip Torr. Controllable text-to-image generation. In *Advances in neural information processing systems (NeurIPS)*, pp. 2063–2073, 2019.

Muyang Li, Ji Lin, Yaoyao Ding, Zhijian Liu, Jun-Yan Zhu, and Song Han. Gan compression: Efficient architectures for interactive conditional gans. In *Conference on Computer Vision and Pattern Recognition (CVPR)*, 2020.

Dong Liang, Rui Wang, Xiaowei Tian, and Cong Zou. Pcgan: Partition-controlled human image generation. In *AAAI Conference on Artificial Intelligence*, volume 33, pp. 8698–8705, 2019.

Ziwei Liu, Ping Luo, Xiaogang Wang, and Xiaoou Tang. Deep learning face attributes in the wild. In *International Conference on Computer Vision (ICCV)*, pp. 3730–3738, 2015.

Yongyi Lu, Yu-Wing Tai, and Chi-Keung Tang. Attribute-guided face generation using conditional cyclegan. In *Proceedings of the European Conference on Computer Vision (ECCV)*, pp. 282–297, 2018.

Mario Lucic, Karol Kurach, Marcin Michalski, Sylvain Gelly, and Olivier Bousquet. Are gans created equal? a large-scale study. In *Advances in neural information processing systems (NeurIPS)*, pp. 700–709, 2018.

Liqian Ma, Xu Jia, Qianru Sun, Bernt Schiele, Tinne Tuytelaars, and Luc Van Gool. Pose guided person image generation. In *Advances in neural information processing systems (NeurIPS)*, pp. 406–416, 2017.

Maxim Maximov, Ismail Elezi, and Laura Leal-Taixé. Ciagan: Conditional identity anonymization generative adversarial networks. In *Conference on Computer Vision and Pattern Recognition (CVPR)*, 2020.

Mehdi Mirza and Simon Osindero. Conditional generative adversarial nets. *arXiv preprint arXiv:1411.1784*, 2014.

Takeru Miyato and Masanori Koyama. cgans with projection discriminator. In *International Conference on Learning Representations (ICLR)*, 2018.

Takeru Miyato, Toshiki Kataoka, Masanori Koyama, and Yuichi Yoshida. Spectral normalization for generative adversarial networks. In *International Conference on Learning Representations (ICLR)*, 2018.

Yuval Netzer, Tao Wang, Adam Coates, Alessandro Bissacco, Bo Wu, and Andrew Y Ng. Reading digits in natural images with unsupervised feature learning. 2011.

S.M. Nikol'skii. *Analysis III: Spaces of Differentiable Functions*. Encyclopaedia of Mathematical Sciences. Springer Berlin Heidelberg, 2013. ISBN 9783662099612.

Augustus Odena, Christopher Olah, and Jonathon Shlens. Conditional image synthesis with auxiliary classifier gans. In *International Conference on Machine Learning (ICML)*, pp. 2642–2651. JMLR. org, 2017.

Taesung Park, Ming-Yu Liu, Ting-Chun Wang, and Jun-Yan Zhu. Semantic image synthesis with spatially-adaptive normalization. In *Conference on Computer Vision and Pattern Recognition (CVPR)*, pp. 2337–2346, 2019.

Deepak Pathak, Philipp Krahenbuhl, Jeff Donahue, Trevor Darrell, and Alexei A Efros. Context encoders: Feature learning by inpainting. In *Conference on Computer Vision and Pattern Recognition (CVPR)*, pp. 2536–2544, 2016.

Tingting Qiao, Jing Zhang, Duanqing Xu, and Dacheng Tao. Mirrorgan: Learning text-to-image generation by redescription. In *Conference on Computer Vision and Pattern Recognition (CVPR)*, pp. 1505–1514, 2019.

Tim Salimans, Ian Goodfellow, Wojciech Zaremba, Vicki Cheung, Alec Radford, and Xi Chen. Improved techniques for training gans. In *Advances in neural information processing systems (NeurIPS)*, pp. 2234–2242, 2016.

Yoan Shin and Joydeep Ghosh. The pi-sigma network: An efficient higher-order neural network for pattern classification and function approximation. In *International Joint Conference on Neural Networks*, volume 1, pp. 13–18, 1991.

Aliaksandr Siarohin, Enver Sangineto, Stephane Lathuiliere, and Nicu Sebe. Deformable gans for pose-based human image generation. In *Conference on Computer Vision and Pattern Recognition (CVPR)*, pp. 3408–3416, 2018.

Rewa Sood, Binit Topiwala, Karthik Choutagunta, Rohit Sood, and Mirabela Rusu. An application of generative adversarial networks for super resolution medical imaging. In *International Conference on Machine Learning and Applications (ICMLA)*, pp. 326–331, 2018.

Marshall H Stone. The generalized weierstrass approximation theorem. *Mathematics Magazine*, 21 (5):237–254, 1948.

Christian Szegedy, Wei Liu, Yangqing Jia, Pierre Sermanet, Scott Reed, Dragomir Anguelov, Dumitru Erhan, Vincent Vanhoucke, and Andrew Rabinovich. Going deeper with convolutions. In *Conference on Computer Vision and Pattern Recognition (CVPR)*, pp. 1–9, 2015.

Lucas Theis, Aäron van den Oord, and Matthias Bethge. A note on the evaluation of generative models. In *International Conference on Learning Representations (ICLR)*, 2016.

Luan Tran, Xi Yin, and Xiaoming Liu. Disentangled representation learning gan for pose-invariant face recognition. In *Conference on Computer Vision and Pattern Recognition (CVPR)*, volume 3, pp. 7, 2017.

Ting-Chun Wang, Ming-Yu Liu, Jun-Yan Zhu, Guilin Liu, Andrew Tao, Jan Kautz, and Bryan Catanzaro. Video-to-video synthesis. In *Advances in neural information processing systems (NeurIPS)*, 2018a.

Ting-Chun Wang, Ming-Yu Liu, Jun-Yan Zhu, Andrew Tao, Jan Kautz, and Bryan Catanzaro. High-resolution image synthesis and semantic manipulation with conditional gans. In *Conference on Computer Vision and Pattern Recognition (CVPR)*, pp. 8798–8807, 2018b.

Bingzhe Wu, Haodong Duan, Zhichao Liu, and Guangyu Sun. Srpgan: Perceptual generative adversarial network for single image super resolution. *arXiv preprint arXiv:1712.05927*, 2017a.

Huikai Wu, Shuai Zheng, Junge Zhang, and Kaiqi Huang. Gp-gan: Towards realistic high-resolution image blending. In *Proceedings of the 27th ACM International Conference on Multimedia*, pp. 2487–2495, 2019.

Xian Wu, Kun Xu, and Peter Hall. A survey of image synthesis and editing with generative adversarial networks. *Tsinghua Science and Technology*, 22(6):660–674, 2017b.

You Xie, Erik Franz, Mengyu Chu, and Nils Thuerey. tempogan: A temporally coherent, volumetric gan for super-resolution fluid flow. *ACM Transactions on Graphics (TOG)*, 37(4):1–15, 2018.

Tao Xu, Pengchuan Zhang, Qiuyuan Huang, Han Zhang, Zhe Gan, Xiaolei Huang, and Xiaodong He. Attngan: Fine-grained text to image generation with attentional generative adversarial networks. In *Conference on Computer Vision and Pattern Recognition (CVPR)*, pp. 1316–1324, 2018.

Xiangyu Xu, Deqing Sun, Jinshan Pan, Yujin Zhang, Hanspeter Pfister, and Ming-Hsuan Yang. Learning to super-resolve blurry face and text images. In *International Conference on Computer Vision (ICCV)*, pp. 251–260, 2017.

Qiaojing Yan and Wei Wang. Dcgans for image super-resolution, denoising and debluring. *Advances in neural information processing systems (NeurIPS)*, pp. 487–495, 2017.

Chenyu You, Guang Li, Yi Zhang, Xiaoliu Zhang, Hongming Shan, Mengzhou Li, Shenghong Ju, Zhen Zhao, Zhuiyang Zhang, Wenxiang Cong, et al. Ct super-resolution gan constrained by the identical, residual, and cycle learning ensemble (gan-circle). *IEEE Transactions on Medical Imaging*, 39(1):188–203, 2019.

Jiahui Yu, Zhe Lin, Jimei Yang, Xiaohui Shen, Xin Lu, and Thomas S Huang. Generative image inpainting with contextual attention. In *Conference on Computer Vision and Pattern Recognition (CVPR)*, pp. 5505–5514, 2018a.

Xin Yu, Basura Fernando, Richard Hartley, and Fatih Porikli. Super-resolving very low-resolution face images with supplementary attributes. In *Conference on Computer Vision and Pattern Recognition (CVPR)*, pp. 908–917, 2018b.

Fangneng Zhan, Hongyuan Zhu, and Shijian Lu. Spatial fusion gan for image synthesis. In *Conference on Computer Vision and Pattern Recognition (CVPR)*, pp. 3653–3662, 2019.

Han Zhang, Tao Xu, Hongsheng Li, Shaoting Zhang, Xiaogang Wang, Xiaolei Huang, and Dimitris N Metaxas. Stackgan++: Realistic image synthesis with stacked generative adversarial networks. *IEEE Transactions on Pattern Analysis and Machine Intelligence (T-PAMI)*, 41(8):1947–1962, 2018.

Han Zhang, Ian Goodfellow, Dimitris Metaxas, and Augustus Odena. Self-attention generative adversarial networks. In *International Conference on Machine Learning (ICML)*, 2019.

Shengjia Zhao, Hongyu Ren, Arianna Yuan, Jiaming Song, Noah Goodman, and Stefano Ermon. Bias and generalization in deep generative models: An empirical study. In *Advances in neural information processing systems (NeurIPS)*, pp. 10792–10801, 2018.

Jun-Yan Zhu, Taesung Park, Phillip Isola, and Alexei A Efros. Unpaired image-to-image translation using cycle-consistent adversarial networks. In *International Conference on Computer Vision (ICCV)*, pp. 2223–2232, 2017.

A Summary of sections in the Appendix

In the following sections, further details and derivations are provided to elaborate the details of the MVP. Specifically, in sec. B the decomposition and related details on the method are developed. The extension of our method beyond two-input variables is studied in sec. C. A method frequently used in the literature for fusing information is concatenation; we analyze how concatenation captures only additive and not more complex correlations (e.g., multiplicative) in sec. D. The two methods that are closest to our work are Π-Net (Chrysos et al., 2020) and SPADE (Park et al., 2019). An analysis of the differences from each methods are developed in sec. E and sec. F respectively. The experimental details including the evaluation metrics and details on the baselines are developed in sec. G. In sec. H, additional experimental results are included.

B METHOD DERIVATIONS

In this section, we expand on the method details, including the scalar output case or the notation. Specifically, a more detailed notation is determined in sec. B.1; the scalar output case is analyzed in sec. B.2. In sec. B.3 a second order expansion is assumed to illustrate the connection between the polynomial expansion and the recursive formula. Sequentially, we derive an *alternative* model with different factor sharing. This model, called Nested-MVP, has a nested factor sharing format (sec. B.4).

B.1 NOTATION

Our derivations rely on tensors (i.e., multidimensional equivalent of matrices) and (tensor) products. We relay below the core notation used in our work, the interested reader can find further information in the tensor-related literature (Kolda & Bader, 2009; Debals & De Lathauwer, 2017).

Symbols of variables: Tensors/matrices/vectors are symbolized by calligraphic/uppercase/lowercase boldface letters e.g., $\boldsymbol{\mathcal{W}}$,$\boldsymbol{W}$,$\boldsymbol{w}$.

Matrix products: The *Hadamard* product of $\boldsymbol{A}, \boldsymbol{B} \in \mathbb{R}^{I \times N}$ is defined as $\boldsymbol{A} * \boldsymbol{B}$ and is equal to $a_{(i,j)} b_{(i,j)}$ for the (i, j) element. The *Khatri-Rao* product of matrices $\boldsymbol{A} \in \mathbb{R}^{I \times N}$ and $\boldsymbol{B} \in \mathbb{R}^{J \times N}$ is denoted by $\boldsymbol{A} \odot \boldsymbol{B}$ and yields a matrix of dimensions $(IJ) \times N$. The Khatri-Rao product for a set of matrices $\{\boldsymbol{A}_{[m]} \in \mathbb{R}^{I_m \times N}\}_{m=1}^{M}$ is abbreviated by $\boldsymbol{A}_{[1]} \odot \boldsymbol{A}_{[2]} \odot \cdots \odot \boldsymbol{A}_{[M]} \doteq \bigodot_{m=1}^{M} \boldsymbol{A}_{[m]}$.

Tensors: Each element of an Mth order tensor $\boldsymbol{\mathcal{W}}$ is addressed by M indices, i.e., $(\boldsymbol{\mathcal{W}})_{i_1,i_2,\ldots,i_M} \doteq w_{i_1,i_2,\ldots,i_M}$. An Mth-order tensor $\boldsymbol{\mathcal{W}}$ is defined over the tensor space $\mathbb{R}^{I_1 \times I_2 \times \cdots \times I_M}$, where $I_m \in \mathbb{Z}$ for $m = 1, 2, \ldots, M$. The *mode-m unfolding* of a tensor $\boldsymbol{\mathcal{W}} \in \mathbb{R}^{I_1 \times I_2 \times \cdots \times I_M}$ maps $\boldsymbol{\mathcal{W}}$ to a matrix $\boldsymbol{W}_{(m)} \in \mathbb{R}^{I_m \times \bar{I}_m}$ with $\bar{I}_m = \prod_{\substack{k=1 \\ k \neq m}}^{M} I_k$ such that the tensor element $w_{i_1,i_2,\ldots,i_M}$ is mapped to the matrix element $w_{i_m,j}$ where $j = 1 + \sum_{\substack{k=1 \\ k \neq m}}^{M} (i_k - 1) J_k$ with $J_k = \prod_{\substack{n=1 \\ n \neq m}}^{k-1} I_n$. The *mode-$m$ vector product* of $\boldsymbol{\mathcal{W}}$ with a vector $\boldsymbol{u} \in \mathbb{R}^{I_m}$, denoted by $\boldsymbol{\mathcal{W}} \times_m \boldsymbol{u} \in \mathbb{R}^{I_1 \times I_2 \times \cdots \times I_{m-1} \times I_{m+1} \times \cdots \times I_M}$, results in a tensor of order $M - 1$:

$$(\boldsymbol{\mathcal{W}} \times_m \boldsymbol{u})_{i_1,\ldots,i_{m-1},i_{m+1},\ldots,i_M} = \sum_{i_m=1}^{I_m} w_{i_1,i_2,\ldots,i_M} u_{i_m}. \tag{3}$$

We denote $\boldsymbol{\mathcal{W}} \times_1 \boldsymbol{u}^{(1)} \times_2 \boldsymbol{u}^{(2)} \times_3 \cdots \times_M \boldsymbol{u}^{(M)} \doteq \boldsymbol{\mathcal{W}} \prod_{m=1}^{m} \times_m \boldsymbol{u}^{(m)}$.

The *CP decomposition* (Kolda & Bader, 2009) factorizes a tensor into a sum of component rank-one tensors. The rank-R CP decomposition of an Mth-order tensor $\boldsymbol{\mathcal{W}}$ is written as:

$$\boldsymbol{\mathcal{W}} \doteq [\![\boldsymbol{U}_{[1]}, \boldsymbol{U}_{[2]}, \ldots, \boldsymbol{U}_{[M]}]\!] = \sum_{r=1}^{R} \boldsymbol{u}_r^{(1)} \circ \boldsymbol{u}_r^{(2)} \circ \cdots \circ \boldsymbol{u}_r^{(M)}, \tag{4}$$

where $\circ$ is the vector outer product. The factor matrices $\big\{\boldsymbol{U}_{[m]} = [\boldsymbol{u}_1^{(m)}, \boldsymbol{u}_2^{(m)}, \cdots, \boldsymbol{u}_R^{(m)}] \in \mathbb{R}^{I_m \times R}\big\}_{m=1}^{M}$ collect the vectors from the rank-one components. By considering the mode-1 unfolding of $\boldsymbol{\mathcal{W}}$, the CP decomposition can be written in matrix form as:

$$\boldsymbol{W}_{(1)} \doteq \boldsymbol{U}_{[1]} \Bigg(\bigodot_{m=M}^{2} \boldsymbol{U}_{[m]} \Bigg)^T \tag{5}$$

The following lemma is useful in our method:

Lemma 1. *For a set of N matrices $\{\boldsymbol{A}_{[\nu]} \in \mathbb{R}^{I_\nu \times K}\}_{\nu=1}^{N}$ and $\{\boldsymbol{B}_{[\nu]} \in \mathbb{R}^{I_\nu \times L}\}_{\nu=1}^{N}$, the following equality holds:*

$$(\bigodot_{\nu=1}^{N} \boldsymbol{A}_{[\nu]})^T \cdot (\bigodot_{\nu=1}^{N} \boldsymbol{B}_{[\nu]}) = (\boldsymbol{A}_{[1]}^T \cdot \boldsymbol{B}_{[1]}) * \ldots * (\boldsymbol{A}_{[N]}^T \cdot \boldsymbol{B}_{[N]}) \tag{6}$$

An indicative proof can be found in the Appendix of Chrysos et al. (2019).

$$x_\tau = \begin{bmatrix} w^{[1,1]}_{\tau,1}, w^{[1,1]}_{\tau,2}, \cdots, w^{[1,1]}_{\tau,d} \end{bmatrix} \begin{bmatrix} z_{II,1} \\ \vdots \\ z_{II,d} \end{bmatrix} + \begin{bmatrix} w^{[1,2]}_{\tau,1}, w^{[1,2]}_{\tau,2}, \cdots, w^{[1,2]}_{\tau,d} \end{bmatrix} \begin{bmatrix} z_{I,1} \\ \vdots \\ z_{I,d} \end{bmatrix} + \begin{bmatrix} \cdots & z_{II,\lambda} & \cdots \end{bmatrix} \begin{bmatrix} w^{[2,1]}_{\tau,\lambda,\mu} \end{bmatrix} \begin{bmatrix} \vdots \\ z_{II,\mu} \\ \vdots \end{bmatrix} +$$

$$\begin{bmatrix} \cdots & z_{I,\lambda} & \cdots \end{bmatrix} \begin{bmatrix} w^{[2,3]}_{\tau,\lambda,\mu} \end{bmatrix} \begin{bmatrix} \vdots \\ z_{I,\mu} \\ \vdots \end{bmatrix} + \begin{bmatrix} \cdots & z_{I,\lambda} & \cdots \end{bmatrix} \begin{bmatrix} w^{[2,2]}_{\tau,\lambda,\mu} \end{bmatrix} \begin{bmatrix} \vdots \\ z_{II,\mu} \\ \vdots \end{bmatrix}$$

Figure 5: Schematic for second order expansion with scalar output $x_\tau \in \mathbb{R}$. The abbreviations $z_{I,\lambda}, z_{I,\mu}$ are elements of $\boldsymbol{z}_I$ with $\lambda, \mu \in [1, d]$. Similarly, $z_{II,\lambda}, z_{II,\mu}$ are elements of $\boldsymbol{z}_{II}$. The first two terms (on the right side of the equation) are the first-order correlations; the next two terms are the second order auto-correlations. The last term expresses the second order cross-correlations.

B.2 Scalar output

The proposed formulation expresses higher-order interactions of the input variables. To elaborate that, we develop the single output case below. That is, we focus on an element τ of the output vector, e.g., a single pixel. In the next few paragraphs, we consider the case of a scalar output x_τ, with $\tau \in [1, o]$ when the input variables are $\boldsymbol{z}_{\text{I}}, \boldsymbol{z}_{\text{II}} \in \mathbb{K}^d$. To avoid cluttering the notation we only refer to the scalar output with x_τ in the next few paragraphs.

As a reminder, the polynomial of expansion order $N \in \mathbb{N}$ with output $\boldsymbol{x} \in \mathbb{R}^o$ has the form:

$$\boldsymbol{x} = G(\boldsymbol{z}_{\text{I}}, \boldsymbol{z}_{\text{II}}) = \sum_{n=1}^{N} \sum_{\rho=1}^{n+1} \left(\boldsymbol{\mathcal{W}}^{[n,\rho]} \prod_{j=2}^{\rho} \times_j \boldsymbol{z}_{\text{I}} \prod_{\tau=\rho+1}^{n+1} \times_\tau \boldsymbol{z}_{\text{II}} \right) + \boldsymbol{\beta} \tag{7}$$

We assume a second order expansion ($N = 2$) and let τ denote an arbitrary scalar output of $\boldsymbol{x}$. The first order correlations can be expressed through the sums $\sum_{\lambda=1}^{d} w^{[1,1]}_{\tau,\lambda} z_{\text{II},\lambda}$ and $\sum_{\lambda=1}^{d} w^{[1,2]}_{\tau,\lambda} z_{\text{I},\lambda}$. The second order correlations include both auto- and cross-correlations. The tensors $\boldsymbol{\mathcal{W}}^{[2,1]}$ and $\boldsymbol{\mathcal{W}}^{[2,3]}$ capture the auto-correlations, while the tensor $\boldsymbol{\mathcal{W}}^{[2,2]}$ captures the cross-correlations.

A pictorial representation of the correlations are captured in Fig. 5. Collecting all the terms in an equation, each output is expressed as:

$$x_\tau = \beta_\tau + \sum_{\lambda=1}^{d} \left[w^{[1,1]}_{\tau,\lambda} z_{\text{II},\lambda} + w^{[1,2]}_{\tau,\lambda} z_{\text{I},\lambda} + \sum_{\mu=1}^{d} w^{[2,1]}_{\tau,\lambda,\mu} z_{\text{II},\lambda} z_{\text{II},\mu} + \sum_{\mu=1}^{d} w^{[2,3]}_{\tau,\lambda,\mu} z_{\text{I},\lambda} z_{\text{I},\mu} + \sum_{\mu=1}^{d} w^{[2,2]}_{\tau,\lambda,\mu} z_{\text{I},\lambda} z_{\text{II},\mu} \right] \tag{8}$$

where $\beta_\tau \in \mathbb{R}$. Notice that all the correlations of up to second order are captured in equation 8.

B.3 Second order derivation for two-variable input

In all our derivations, the variables associated with the first input $\boldsymbol{z}_{\text{I}}$ have an I notation, e.g., $\boldsymbol{U}_{[1,I]}$. Respectively for the second input $\boldsymbol{z}_{\text{II}}$, the notation II is used.

Even though equation 7 enables any order of expansion, the learnable parameters increase exponentially, therefore we can use a coupled factorization to reduce the parameters. Next, we derive the factorization for a second order expansion (i.e., $N = 2$) and then provide the recursive relationship that generalizes it for an arbitrary order.

Second order derivation: For a second order expansion (i.e., $N = 2$ in equation 1), we factorize each parameter tensor $\boldsymbol{\mathcal{W}}^{[n,\rho]}$. We assume a coupled CP decomposition for each parameter as follows:

- Let $\boldsymbol{W}^{[1,1]}_{(1)} = \boldsymbol{C}\boldsymbol{U}^T_{[1,II]}$ and $\boldsymbol{W}^{[1,2]}_{(1)} = \boldsymbol{C}\boldsymbol{U}^T_{[1,I]}$ be the parameters for $n = 1$.
- Let $\boldsymbol{W}^{[2,1]}_{(1)} = \boldsymbol{C}(\boldsymbol{U}_{[2,II]} \odot \boldsymbol{U}_{[1,II]})^T$ and $\boldsymbol{W}^{[2,3]}_{(1)} = \boldsymbol{C}(\boldsymbol{U}_{[2,I]} \odot \boldsymbol{U}_{[1,I]})^T$ capture the second order correlations of a single variable ($\boldsymbol{z}_{\text{II}}$ and $\boldsymbol{z}_{\text{I}}$ respectively).

- The cross-terms are expressed in $\boldsymbol{\mathcal{W}}^{[2,2]} \times_2 \boldsymbol{z}_{\text{I}} \times_3 \boldsymbol{z}_{\text{II}}$. The output of the τ element[2] is $\sum_{\lambda,\mu=1}^{d} w_{\tau,\lambda,\mu}^{[2,2]} z_{\text{I},\lambda} z_{\text{II},\mu}$. The product $\hat{\boldsymbol{\mathcal{W}}}^{[2,2]} \times_2 \boldsymbol{z}_{\text{II}} \times_3 \boldsymbol{z}_{\text{I}}$ also results in the same elementwise expression. Hence, to allow for symmetric expression, we factorize the term $\boldsymbol{W}_{(1)}^{[2,2]}$ as the sum of the two terms $\boldsymbol{C}(\boldsymbol{U}_{[2,II]} \odot \boldsymbol{U}_{[1,I]})^T$ and $\boldsymbol{C}(\boldsymbol{U}_{[2,I]} \odot \boldsymbol{U}_{[1,II]})^T$. For each of the two terms, we assume that the vector-valued inputs are accordingly multiplied.

The parameters $\boldsymbol{C} \in \mathbb{R}^{o \times k}, \boldsymbol{U}_{[m,\phi]} \in \mathbb{R}^{d \times k}$ ($m = 1, 2$ and $\phi = \{I, II\}$) are learnable. The aforementioned factorization results in the following equation:

$$\boldsymbol{x} = \boldsymbol{C}\boldsymbol{U}_{[1,II]}^T \boldsymbol{z}_{\text{II}} + \boldsymbol{C}\boldsymbol{U}_{[1,I]}^T \boldsymbol{z}_{\text{I}} + \boldsymbol{C}\Big(\boldsymbol{U}_{[2,II]} \odot \boldsymbol{U}_{[1,II]}\Big)^T \Big(\boldsymbol{z}_{\text{II}} \odot \boldsymbol{z}_{\text{II}}\Big) + \boldsymbol{C}\Big(\boldsymbol{U}_{[2,I]} \odot \boldsymbol{U}_{[1,I]}\Big)^T \Big(\boldsymbol{z}_{\text{I}} \odot \boldsymbol{z}_{\text{I}}\Big) + \boldsymbol{C}\Big(\boldsymbol{U}_{[2,I]} \odot \boldsymbol{U}_{[1,II]}\Big)^T \Big(\boldsymbol{z}_{\text{I}} \odot \boldsymbol{z}_{\text{II}}\Big) + \boldsymbol{C}\Big(\boldsymbol{U}_{[2,II]} \odot \boldsymbol{U}_{[1,I]}\Big)^T \Big(\boldsymbol{z}_{\text{II}} \odot \boldsymbol{z}_{\text{I}}\Big) + \boldsymbol{\beta} \tag{9}$$

This expansion captures the correlations (up to second order) of the two input variables $\boldsymbol{z}_{\text{I}}, \boldsymbol{z}_{\text{II}}$.

To make the proof more complete, we remind the reader that the recursive relationship (i.e., (2) in the main paper) is:

$$\boldsymbol{x}_n = \boldsymbol{x}_{n-1} + \Big(\boldsymbol{U}_{[n,I]}^T \boldsymbol{z}_{\text{I}} + \boldsymbol{U}_{[n,II]}^T \boldsymbol{z}_{\text{II}}\Big) * \boldsymbol{x}_{n-1} \tag{10}$$

for $n = 2, \ldots, N$ with $\boldsymbol{x}_1 = \boldsymbol{U}_{[1,I]}^T \boldsymbol{z}_{\text{I}} + \boldsymbol{U}_{[1,II]}^T \boldsymbol{z}_{\text{II}}$ and $\boldsymbol{x} = \boldsymbol{C}\boldsymbol{x}_N + \boldsymbol{\beta}$.

Claim 1. *The equation (9) is a special format of a polynomial that is visualized as in Fig. 1 of the main paper. Equivalently, prove that (9) follows the recursive relationship of (10).*

Proof. We observe that the first two terms of equation 9 are equal to $\boldsymbol{C}\boldsymbol{x}_1$ (from equation 10). By applying Lemma 1 in the terms that have Khatri-Rao product, we obtain:

$$\begin{aligned} \boldsymbol{x} = \boldsymbol{\beta} + \boldsymbol{C}\boldsymbol{x}_1 + \boldsymbol{C}\Bigg\{ \Big(\boldsymbol{U}_{[2,II]}^T \boldsymbol{z}_{\text{II}}\Big) * \Big(\boldsymbol{U}_{[1,II]}^T \boldsymbol{z}_{\text{II}}\Big) + \Big(\boldsymbol{U}_{[2,I]}^T \boldsymbol{z}_{\text{I}}\Big) * \Big(\boldsymbol{U}_{[1,I]}^T \boldsymbol{z}_{\text{I}}\Big) + \\ \Big(\boldsymbol{U}_{[2,I]}^T \boldsymbol{z}_{\text{I}}\Big) * \Big(\boldsymbol{U}_{[1,II]}^T \boldsymbol{z}_{\text{II}}\Big) + \Big(\boldsymbol{U}_{[2,II]}^T \boldsymbol{z}_{\text{II}}\Big) * \Big(\boldsymbol{U}_{[1,I]}^T \boldsymbol{z}_{\text{I}}\Big) \Bigg\} = \\ \boldsymbol{\beta} + \boldsymbol{C}\boldsymbol{x}_1 + \boldsymbol{C}\Bigg\{ \Big[\Big(\boldsymbol{U}_{[2,I]}^T \boldsymbol{z}_{\text{I}}\Big) + \Big(\boldsymbol{U}_{[2,II]}^T \boldsymbol{z}_{\text{II}}\Big) \Big] * \boldsymbol{x}_1 \Bigg\} = \boldsymbol{C}\boldsymbol{x}_2 + \boldsymbol{\beta} \end{aligned} \tag{11}$$

The last equation is precisely the one that arises from the recursive relationship from equation 10.

□

To prove the recursive formula for the Nth order expansion, a similar pattern as in sec.C of Poly-GAN (Chrysos et al., 2019) can be followed. Specifically, the difference here is that because of the two input variables, the auto- and cross-correlation variables should be included. Other than that, the same factor sharing is followed.

B.4 Nested-MVP model for two-variable input

The model proposed above (i.e., equation 10), relies on a single coupled CP decomposition, however a more flexible model can factorize each level with a CP decomposition. To effectively do that, we utilize learnable hyper-parameters $\boldsymbol{b}_{[n]} \in \mathbb{R}^{\omega}$ for $n \in [1, N]$, which act as scaling factors for each parameter tensor. Then, a polynomial of expansion order $N \in \mathbb{N}$ with output $\boldsymbol{x} \in \mathbb{R}^o$ has the form:

$$\boldsymbol{x} = G(\boldsymbol{z}_{\text{I}}, \boldsymbol{z}_{\text{II}}) = \sum_{n=1}^{N} \sum_{\rho=2}^{n+2} \left(\boldsymbol{\mathcal{W}}^{[n,\rho-1]} \times_2 \boldsymbol{b}_{[N+1-n]} \prod_{j=3}^{\rho} \times_j \boldsymbol{z}_{\text{I}} \prod_{\tau=\rho+1}^{n+2} \times_\tau \boldsymbol{z}_{\text{II}} \right) + \boldsymbol{\beta} \tag{12}$$

[2] An elementwise analysis (with a scalar output) is provided on the Appendix (sec. B.2).

To demonstrate the factorization without cluttering the notation, we assume a second order expansion in equation 12.

Second order derivation: The second order expansion, i.e., $N = 2$, is derived below. We jointy factorize all parameters of equation 12 with a nested decomposition as follows:

- First order parameters : $\boldsymbol{W}_{(1)}^{[1,1]} = \boldsymbol{C}(\boldsymbol{A}_{[2,II]} \odot \boldsymbol{B}_{[2]})^T$ and $\boldsymbol{W}_{(1)}^{[1,2]} = \boldsymbol{C}(\boldsymbol{A}_{[2,I]} \odot \boldsymbol{B}_{[2]})^T$.
- Let $\boldsymbol{W}_{(1)}^{[2,1]} = \boldsymbol{C}\Big\{\boldsymbol{A}_{[2,II]} \odot \Big[\Big(\boldsymbol{A}_{[1,II]} \odot \boldsymbol{B}_{[1]}\Big)\boldsymbol{V}_{[2]}\Big]\Big\}^T$ and $\boldsymbol{W}_{(1)}^{[2,3]} = \boldsymbol{C}\Big\{\boldsymbol{A}_{[2,I]} \odot \Big[\Big(\boldsymbol{A}_{[1,I]} \odot \boldsymbol{B}_{[1]}\Big)\boldsymbol{V}_{[2]}\Big]\Big\}^T$ capture the second order correlations of a single variable ($\boldsymbol{z}_{\text{II}}$ and $\boldsymbol{z}_{\text{I}}$ respectively).
- The cross-terms are included in $\boldsymbol{\mathcal{W}}^{[2,2]} \times_2 \boldsymbol{b}_{[1]} \times_3 \boldsymbol{z}_{\text{I}} \times_4 \boldsymbol{z}_{\text{II}}$. The output of the τ element is expressed as $\sum_{\nu=1}^{\omega}\sum_{\lambda,\mu=1}^{d} w_{\tau,\nu,\lambda,\mu}^{[2,2]} b_{[1],\omega} z_{\text{I},\lambda} z_{\text{II},\mu}$. Similarly, the product $\hat{\boldsymbol{\mathcal{W}}}^{[2,2]} \times_2 \boldsymbol{b}_{[1]} \times_3 \boldsymbol{z}_{\text{II}} \times_4 \boldsymbol{z}_{\text{I}}$ has output $\sum_{\nu=1}^{\omega}\sum_{\lambda,\mu=1}^{d} w_{\tau,\nu,\mu,\lambda}^{[2,2]} b_{[1],\omega} z_{\text{I},\lambda} z_{\text{II},\mu}$ for the τ element. Notice that the only change in the two expressions is the permutation of the third and forth modes of the tensor; the rest of the expression remains the same. Therefore, to account for this symmetry we factorize the term $\boldsymbol{\mathcal{W}}^{[2,2]}$ as the sum of two terms and assume that each term is multiplied by the respective terms. Let $\boldsymbol{W}_{(1)}^{[2,2]} = \boldsymbol{C}\Big\{\boldsymbol{A}_{[2,I]} \odot \Big[\Big(\boldsymbol{A}_{[1,II]} \odot \boldsymbol{B}_{[1]}\Big)\boldsymbol{V}_{[2]}\Big] + \boldsymbol{A}_{[2,II]} \odot \Big[\Big(\boldsymbol{A}_{[1,I]} \odot \boldsymbol{B}_{[1]}\Big)\boldsymbol{V}_{[2]}\Big]\Big\}^T$.

The parameters $\boldsymbol{C} \in \mathbb{R}^{o\times k}, \boldsymbol{A}_{[n,\phi]} \in \mathbb{R}^{d\times k}, \boldsymbol{V}_{[n]} \in \mathbb{R}^{k\times k}, \boldsymbol{B}_{[n]} \in \mathbb{R}^{\omega\times k}$ for $n = 1, 2$ and $\phi = \{I, II\}$ are learnable. Collecting all the terms above and extracting $\boldsymbol{C}$ as a common factor (we ommit $\boldsymbol{C}$ below to avoid cluttering the notation):

$$
\begin{aligned}
&(\boldsymbol{A}_{[2,II]} \odot \boldsymbol{B}_{[2]})^T(\boldsymbol{z}_{\text{II}} \odot \boldsymbol{b}_{[2]}) + (\boldsymbol{A}_{[2,I]} \odot \boldsymbol{B}_{[2]})^T(\boldsymbol{z}_{\text{I}} \odot \boldsymbol{b}_{[2]}) + \\
&\Big\{\boldsymbol{A}_{[2,II]} \odot \Big[\Big(\boldsymbol{A}_{[1,II]} \odot \boldsymbol{B}_{[1]}\Big)\boldsymbol{V}_{[2]}\Big]\Big\}^T(\boldsymbol{z}_{\text{II}} \odot \boldsymbol{z}_{\text{II}} \odot \boldsymbol{b}_{[1]}) + \\
&\Big\{\boldsymbol{A}_{[2,I]} \odot \Big[\Big(\boldsymbol{A}_{[1,I]} \odot \boldsymbol{B}_{[1]}\Big)\boldsymbol{V}_{[2]}\Big]\Big\}^T(\boldsymbol{z}_{\text{I}} \odot \boldsymbol{z}_{\text{I}} \odot \boldsymbol{b}_{[1]}) + \\
&\Big\{\boldsymbol{A}_{[2,I]} \odot \Big[\Big(\boldsymbol{A}_{[1,II]} \odot \boldsymbol{B}_{[1]}\Big)\boldsymbol{V}_{[2]}\Big]\Big\}^T(\boldsymbol{z}_{\text{I}} \odot \boldsymbol{z}_{\text{II}} \odot \boldsymbol{b}_{[1]}) + \\
&\Big\{\boldsymbol{A}_{[2,II]} \odot \Big[\Big(\boldsymbol{A}_{[1,I]} \odot \boldsymbol{B}_{[1]}\Big)\boldsymbol{V}_{[2]}\Big]\Big\}^T(\boldsymbol{z}_{\text{II}} \odot \boldsymbol{z}_{\text{I}} \odot \boldsymbol{b}_{[1]}) = \\
&\Big(\boldsymbol{A}_{[2,II]}^T\boldsymbol{z}_{\text{II}} + \boldsymbol{A}_{[2,I]}^T\boldsymbol{z}_{\text{I}}\Big) * \Big(\boldsymbol{B}_{[2]}^T\boldsymbol{b}_{[2]}\Big) + \\
&\Big(\boldsymbol{A}_{[2,II]}^T\boldsymbol{z}_{\text{II}} + \boldsymbol{A}_{[2,I]}^T\boldsymbol{z}_{\text{I}}\Big) * \Big\{\boldsymbol{V}_{[2]}^T\Big[\Big(\boldsymbol{A}_{[1,II]}^T\boldsymbol{z}_{\text{II}} + \boldsymbol{A}_{[1,I]}^T\boldsymbol{z}_{\text{I}}\Big) * \Big(\boldsymbol{B}_{[1]}^T\boldsymbol{b}_{[1]}\Big)\Big]\Big\}
\end{aligned}
\tag{13}
$$

The last equation is precisely a recursive equation that can be expressed with the Fig. 6 or equivalently the generalized recursive relationship below.

Recursive relationship: The recursive formula for the Nested-MVP model with arbitrary expansion order $N \in \mathbb{N}$ is the following:

$$
\boldsymbol{x}_n = \Big(\boldsymbol{A}_{[n,I]}^T\boldsymbol{z}_{\text{I}} + \boldsymbol{A}_{[n,II]}^T\boldsymbol{z}_{\text{II}}\Big) * \Big(\boldsymbol{V}_{[n]}^T\boldsymbol{x}_{n-1} + \boldsymbol{B}_{[n]}^T\boldsymbol{b}_{[n]}\Big) \tag{14}
$$

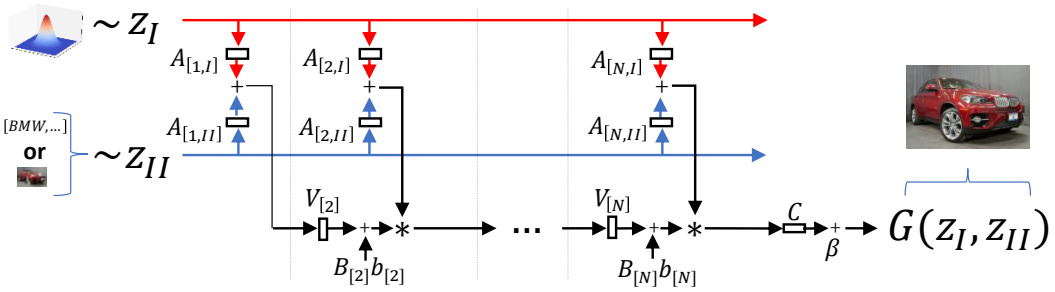

Figure 6: Abstract schematic for N^{th} order approximation of $\boldsymbol{x} = G(\boldsymbol{z}_I, \boldsymbol{z}_{II})$ with Nested-MVP model. The inputs $\boldsymbol{z}_I, \boldsymbol{z}_{II}$ are symmetric in our formulation. We denote with $\boldsymbol{z}_I$ a sample from the noise distribution (e.g., Gaussian), while $\boldsymbol{z}_{II}$ symbolizes a sample from a conditional input (e.g., a class label or a low-resolution image).

where $n \in [2, N]$ and $\boldsymbol{x}_1 = \left(\boldsymbol{A}_{[1,I]}^T \boldsymbol{z}_{\text{I}} + \boldsymbol{A}_{[1,II]}^T \boldsymbol{z}_{\text{II}}\right) * \left(\boldsymbol{B}_{[1]}^T \boldsymbol{b}_{[1]}\right)$. The parameters $\boldsymbol{C} \in \mathbb{R}^{o \times k}, \boldsymbol{A}_{[n,\phi]} \in \mathbb{R}^{d \times k}, \boldsymbol{V}_{[n]} \in \mathbb{R}^{k \times k}, \boldsymbol{B}_{[n]} \in \mathbb{R}^{\omega \times k}$ for $\phi = \{I, II\}$ are learnable. Then, the output $\boldsymbol{x} = \boldsymbol{C}\boldsymbol{x}_N + \boldsymbol{\beta}$.

The Nested-MVP model manifests an alternative network that relies on slightly modified assumptions on the decomposition. Thus, changing the underlying assumptions of the decomposition can modify the resulting network. This can be an important tool for domain-specific applications, e.g., when the domain-knowledge should be inserted in the last layers.

C Beyond two variables

Frequently, more than one conditional inputs are required (Yu et al., 2018b; Xu et al., 2017; Maximov et al., 2020). In such tasks, the aforementioned framework can be generalized to more than two input variables. We demonstrate how this is possible with three variables; then it can trivially extended to an arbitrary number of input variables.

Let $\boldsymbol{z}_{\text{I}}, \boldsymbol{z}_{\text{II}}, \boldsymbol{z}_{\text{III}} \in \mathbb{K}^d$ denote the three input variables. We aim to learn a function that captures the higher-order interactions of the input variables. The polynomial of expansion order $N \in \mathbb{N}$ with output $\boldsymbol{x} \in \mathbb{R}^o$ has the form:

$$\boldsymbol{x} = G(\boldsymbol{z}_{\text{I}}, \boldsymbol{z}_{\text{II}}, \boldsymbol{z}_{\text{III}}) = \sum_{n=1}^{N} \sum_{\rho=1}^{n+1} \sum_{\delta=\rho}^{n+1} \left(\boldsymbol{\mathcal{W}}^{[n,\rho,\delta]} \prod_{j=2}^{\rho} \times_j \boldsymbol{z}_{\text{I}} \prod_{\tau=\rho+1}^{\delta} \times_\tau \boldsymbol{z}_{\text{II}} \prod_{\zeta=\delta+1}^{n+1} \times_\zeta \boldsymbol{z}_{\text{III}} \right) + \boldsymbol{\beta} \tag{15}$$

where $\boldsymbol{\beta} \in \mathbb{R}^o$ and $\boldsymbol{\mathcal{W}}^{[n,\rho,\delta]} \in \mathbb{R}^{o \times \prod_{m=1}^{n} \times_m d}$ (for $n \in [1, N]$ and $\rho, \delta \in [1, n+1]$) are the learnable parameters. As in the two-variable input, the unknown parameters increase exponentially. To that end, we utilize a joint factorization with factor sharing. The recursive relationship of such a factorization is:

$$\boldsymbol{x}_n = \boldsymbol{x}_{n-1} + \left(\boldsymbol{U}_{[n,I]}^T \boldsymbol{z}_{\text{I}} + \boldsymbol{U}_{[n,II]}^T \boldsymbol{z}_{\text{II}} + \boldsymbol{U}_{[n,III]}^T \boldsymbol{z}_{\text{III}} \right) * \boldsymbol{x}_{n-1} \tag{16}$$

for $n = 2, \ldots, N$ with $\boldsymbol{x}_1 = \boldsymbol{U}_{[1,I]}^T \boldsymbol{z}_{\text{I}} + \boldsymbol{U}_{[1,II]}^T \boldsymbol{z}_{\text{II}} + \boldsymbol{U}_{[1,III]}^T \boldsymbol{z}_{\text{III}}$ and $\boldsymbol{x} = \boldsymbol{C}\boldsymbol{x}_N + \boldsymbol{\beta}$.

Notice that the pattern (for each order) is similar to the two-variable input: a) a different embedding is found for each input variable, b) the embeddings are added together, c) the result is multiplied elementwise with the representation of the previous order.

D CONCATENATION OF INPUTS

A popular method used for conditional generation is to concatenate the conditional input with the noise labels. However, as we showcase below, concatenation has two significant drawbacks when compared to our framework. To explain those, we will define a concatenation model.

Let $\boldsymbol{z}_{\text{I}} \in \mathbb{K}_1^{d_1}, \boldsymbol{z}_{\text{II}} \in \mathbb{K}_2^{d_2}$ where $\mathbb{K}_1, \mathbb{K}_2$ can be a subset of real or natural numbers. The output of a concatenation layer is $x = \boldsymbol{P}^T \Big[\boldsymbol{z}_{\text{I}}; \boldsymbol{z}_{\text{II}}\Big]^T$ where the symbol ';' denotes the concatenation and $\boldsymbol{P} \in \mathbb{R}^{(d_1 d_2) \times o}$ is an affine transformation on the concatenated vector. The jth output is $x_j = \sum_{\tau=1}^{d_1} p_{\tau,j} z_{\text{I},\tau} + \sum_{\tau=1}^{d_2} p_{\tau+d_1,j} z_{\text{II},\tau}$.

Therefore, the two differences from the concatenation case are:

- If the input variables are concatenated together we obtain an additive format, not a multiplicative that can capture cross-term correlations. That is, the multiplicative format does allow achieving higher-order auto- and cross- term correlations.
- The concatenation changes the dimensionality of the embedding space. Specifically, the input space has dimensionality $d_1 \cdot d_2$. That has a significant toll on the size of the filters (i.e., it increases the learnable parameters), while still having an additive impact. On the contrary, our framework does not change the dimensionality of the embedding spaces.

E IN-DEPTH DIFFERENCES FROM Π-NET

In the next few paragraphs, we conduct an in-depth analysis of the differences between Π-Net and MVP. The analysis assumes knowledge of the proposed model, i.e., (2).

Chrysos et al. (2020) introduce Π-Net as a polynomial expansion of a single input variable. Their goal is to model functions $\boldsymbol{x} = G(\boldsymbol{z})$ as high-order polynomial expansions of $\boldsymbol{z}$. Their focus is towards using a single-input variable $\boldsymbol{z}$, which can be noise in case of image generation or an image in discriminative experiments. The authors express the StyleGAN architecture (Karras et al., 2019) as a polynomial expansion, while they advocate that the impressive results can be attributed to the polynomial expansion.

To facilitate the in-depth analysis, the recursive relationship that corresponds to (2) is provided below. An Nth order expansion in Π-Net is expressed as:

$$\boldsymbol{x}_n = \Big(\boldsymbol{\Lambda}_{[n]}^T \boldsymbol{z}\Big) * \boldsymbol{x}_{n-1} + \boldsymbol{x}_{n-1} \tag{17}$$

for $n = 2, \dots, N$ with $\boldsymbol{x}_1 = \boldsymbol{\Lambda}_{[1]}^T \boldsymbol{z}$ and $\boldsymbol{x} = \boldsymbol{\Gamma} \boldsymbol{x}_N + \boldsymbol{\beta}$. The parameters $\boldsymbol{\Lambda}, \boldsymbol{\Gamma}$ are learnable.

In this work, we focus on conditional data generation, i.e., there are multiple input variables available as auxiliary information. The trivial application of Π-Net would be to concatenate all the M input variables $\boldsymbol{z}_{\text{I}}, \boldsymbol{z}_{\text{II}}, \boldsymbol{z}_{\text{III}}, \dots$. The input variable $\boldsymbol{z}$ becomes $\boldsymbol{z} = \Big[\boldsymbol{z}_{\text{I}}; \boldsymbol{z}_{\text{II}}; \boldsymbol{z}_{\text{III}}; \dots\Big]$, where the symbol ';' denotes the concatenation. Then, the polynomial expansion of Π-Net can be learned on the concatenated $\boldsymbol{z}$. However, there are four significant reasons that we believe that this is not as flexible as the proposed MVP.

When we refer to Π-Net below, we refer to the model with concatenated input. In addition, let $\boldsymbol{z}_{\text{I}} \in \mathbb{K}_1^{d_1}, \boldsymbol{z}_{\text{II}} \in \mathbb{K}_2^{d_2}$ denote the input variables where $\mathbb{K}_1, \mathbb{K}_2$ can be a subset of real or natural numbers.

Parameter sharing: MVP allows additional flexibility in the structure of the architecture, since MVP utilizes a different projection layer for each input variable. We utilize this flexibility to share the parameters of the conditional input variable; as we detail in (19), we set $\boldsymbol{U}_{[n,II]} = \boldsymbol{U}_{[1,II]}$ on (2). If we want to perform a similar sharing in Π-Net, the formulation equivalent to (17) would be $(\lambda_{[n]})_i = (\lambda_{[1]})_i$ for $i = d_1, \dots, d_1 + d_2$. However, sharing only part of the matrix might be challenging. Additionally, when $\boldsymbol{\Lambda}$ is a convolution, the sharing pattern is not straightforward to be computed. Therefore, MVP enables additional flexibility to the model, which is hard to be included in Π-Net.

Inductive bias: The inductive bias is crucial in machine learning (Zhao et al., 2018), however concatenating the variables restricts the flexibility of the model (i.e. Π-Net). To illustrate that, let us use the super-resolution experiments as an example. The input variable $\boldsymbol{z}_{\text{I}}$ is the noise vector and $\boldsymbol{z}_{\text{II}}$ is the (vectorized) low-resolution image. If we concatenate the two variables, then we should use a fully-connected (dense) layer, which does not model well the spatial correlations. Instead, with MVP, we use a fully-connected layer for the noise vector and a convolution for $\boldsymbol{z}_{\text{II}}$ (low-resolution image). The convolution reduces the number of parameters and captures the spatial correlations in the image. Thus, by concatenating the variables, we reduce the flexibility of the model.

Dimensionality of the inputs: The dimensionality of the inputs might vary orders of magnitude, which might create an imbalance during learning. For instance, in class-conditional generation concatenating the one-hot labels in the input does not scale well when there are hundreds of classes (Odena et al., 2017). We observe a similar phenomenon in class-conditional generation: in Cars196 (with 196 classes) the performance of Π-Net deteriorates considerably when compared to its (relative) performance in CIFAR10 (with 10 classes). On the contrary, MVP does not fuse the elements of the input variables directly, but it projects them into a subspace appropriate for adding them.

Order of expansion with respect to each variable: Frequently, the two inputs do not require the same order of expansion. Without loss of generality, assume that we need correlations up to N_I and N_{II} order (with $N_I < N_{II}$) from $\boldsymbol{z}_{\text{I}}$ and $\boldsymbol{z}_{\text{II}}$ respectively. MVP includes a different transformation for each variable, i.e., $\boldsymbol{U}_{[n,I]}$ for $\boldsymbol{z}_{\text{I}}$ and $\boldsymbol{U}_{[n,II]}$ for $\boldsymbol{z}_{\text{II}}$. Then, we can set $\boldsymbol{U}_{[n,I]} = 0$ for $n > N_I$. On the contrary, the concatenation of inputs (in Π-Net) constrains the expansion to have the same order with respect to each variable.

All in all, we can use concatenation to fuse variables and use Π-Net, however an inherently multivariate model is more flexible and can better encode the types of inductive bias required for conditional data generation.

F In-depth differences from SPADE

In the next few paragraphs, we conduct an in-depth analysis of the differences between SPADE and MVP.

Park et al. (2019) introduce a spatially-adaptive normalization, i.e., SPADE, to improve semantic image synthesis. Their model, referred to as SPADE in the remainder of this work, assumes a semantic layout as a conditional input that facilitates the image generation.

The nth model block applies a normalization on the representation $\boldsymbol{x}_{n-1}$ of the previous layer and then it performs an elementwise multiplication with a transformed semantic layout. The transformed semantic layout can be denoted as $\boldsymbol{A}^T_{[n,II]}\boldsymbol{z}_{\text{II}}$ where $\boldsymbol{z}_{\text{II}}$ denotes the conditional input to the generator. The output of this elementwise multiplication is then propagated to the next model block that performs the same operations. Stacking N such blocks results in an Nth order polynomial expansion which is expressed as:

$$\boldsymbol{x}_n = \left(\boldsymbol{A}^T_{[n,II]}\boldsymbol{z}_{\text{II}}\right) * \left(\boldsymbol{V}^T_{[n]}\boldsymbol{x}_{n-1} + \boldsymbol{B}^T_{[n]}\boldsymbol{b}_{[n]}\right) \tag{18}$$

where $n \in [2, N]$ and $\boldsymbol{x}_1 = \boldsymbol{A}^T_{[1,I]}\boldsymbol{z}_{\text{I}}$. The parameters $\boldsymbol{C} \in \mathbb{R}^{o\times k}, \boldsymbol{A}_{[n,\phi]} \in \mathbb{R}^{d\times k}, \boldsymbol{V}_{[n]} \in \mathbb{R}^{k\times k}, \boldsymbol{B}_{[n]} \in \mathbb{R}^{\omega\times k}$ for $\phi = \{I, II\}$ are learnable. Then, the output $\boldsymbol{x} = \boldsymbol{C}\boldsymbol{x}_N + \boldsymbol{\beta}$.

SPADE as expressed in (18) resembles one of the proposed models of MVP (specifically (14)). In particular, it expresses a polynomial with respect to the conditional variable. The parameters $\boldsymbol{A}_{[n,I]}$ are set as zero, which means that there are no higher-order correlations with respect to the input variable $\boldsymbol{z}_{\text{I}}$. Therefore, our work bears the following differences from Park et al. (2019):

- SPADE proposes a normalization scheme that is only applied to semantic image generation. On the contrary, our proposed MVP can be applied to any conditional data generation task, e.g., class-conditional generation or image-to-image translation.

- **SPADE is a special case of MVP**. In particular, by setting i) $\boldsymbol{A}_{[1,II]}$ equal to zero, ii) $\boldsymbol{A}_{[n,I]}$ in (14) equal to zero, we obtain SPADE. In addition, MVP allows different assumptions on the decompositions which lead to an alternative structure, such as (2).
- SPADE proposes a polynomial expansion with respect to a single variable. On the other hand, our model can extend to an arbitrary number of input variables to account for auxiliary labels, e.g., (16).
- Even though SPADE models higher-order correlations of the conditional variable, it still does not leverage the higher-order correlations of the representations (e.g., as in the product of polynomials) and hence without activation functions it might not work as well as the two-variable expansion.

Park et al. (2019) exhibit impressive generation results with large-scale computing (i.e., they report results using NVIDIA DGX with 8 V100 GPUs). Our goal is not to compete in computationally heavy, large-scale experiments, but rather to illustrate the benefits of the generic formulation of MVP.

SPADE is an important baseline for our work. In particular, we augment SPADE in wo ways: a) by extending it to accept both continuous and discrete variables in $\boldsymbol{z}_{\text{II}}$ and b) by adding polynomial terms with respect to the input variable $\boldsymbol{z}_{\text{I}}$. The latter model is referred to as SPADE-MVP (details on the next section).

G EXPERIMENTAL DETAILS

Metrics: The two most popular metrics (Lucic et al., 2018; Creswell et al., 2018) for evaluation of the synthesized images are the Inception Score (IS) (Salimans et al., 2016) and the Frechet Inception Distance (FID) (Heusel et al., 2017). The metrics utilize the pretrained Inception network (Szegedy et al., 2015) to extract representations of the synthesized images. FID assumes that the representations extracted follow a Gaussian distribution and matches the statistics (i.e., mean and variance) of the representations between real and synthesized samples. Alternative evaluation metrics have been reported as inaccurate, e.g., in Theis et al. (2016), thus we use the IS and FID. Following the standard practice of the literature, the IS is computed by synthesizing $5,000$ samples, while the FID is computed using $10,000$ samples.

The IS is used exclusively for images of natural scenes as a metric. The reasoning behind that is that the Inception network has been trained on images of natural scenes. On the contrary, the FID metric relies on the first and second-order moments of the representations, which are considered more robust to different types of images. Hence, we only report IS for the CIFAR10 related experiments, while for the rest the FID is reported.

Dataset details: There are five main datasets used in this work:

- Large-scale CelebFaces Attributes (or *CelebA* for short) (Liu et al., 2015) is a large-scale face attributes dataset with $202,000$ celebrity images. We use $160,000$ images for training our method.
- *Cars196* (Krause et al., 2013) is a dataset that includes different models of cars in different positions and backgrounds. Cars196 has $16,000$ images, while the images have substantially more variation than CelebA faces.
- *CIFAR10* (Krizhevsky et al., 2014) contains $60,000$ images of natural scenes. Each image is of resolution $32 \times 32 \times 3$ and is classified in one of the 10 classes. CIFAR10 is frequently used as a benchmark for image generation.
- The Street View House Numbers dataset (or *SVHN* for short) (Netzer et al., 2011) has $100,000$ images of digits ($73,257$ of which for training). SVHN includes color house-number images which are classified in 10 classes; each class corresponds to a digit 0 to 9. SVHN images are diverse (e.g., with respect to background, scale).
- *MNIST* (LeCun et al., 1998) consists of images with handwritten digits. Each images depicts a single digit (annotated from 0 to 9) in a 28×28 resolution. The dataset includes $60,000$ images for training.

All the images of CelebA and Cars196 are resized to 64×64 resolution.

Architectures: The discriminator structure is left the same for each experiment, we focus only on the generator architecture. All the architectures are based on two different generator schemes, i.e., the SNGAN (Miyato & Koyama, 2018) and the polynomial expansion of Chrysos et al. (2020) that does not include activation functions in the generator.

The variants of the generator of SNGAN are described below:

- **SNGAN** (Miyato & Koyama, 2018): The generator consists of a convolution, followed by three residual blocks. The discriminator is also based on successive residual blocks. The public implementation of SNGAN with conditional batch normalization (CBN) is used as the baseline.
- **SNGAN-MVP** [proposed]: We convert the resnet-based generator of SNGAN to an MVP model. To obtain MVP, the SNGAN is modified in two ways: a) the Conditional Batch Normalization (CBN) is converted into batch normalization (Ioffe & Szegedy, 2015), b) the injections of the two embeddings (from the inputs) are added after each residual block, i.e. the formula of (2). In other words, the generator is converted to a product of two-variable polynomials.
- **SNGAN-CONC**: Based on SNGAN-MVP, we replace each Hadamard product with a concatenation. This implements the variant mentioned in sec. D.
- **SNGAN-SPADE** (Park et al., 2019): As described in sec. F, SPADE is a polynomial with respect to the conditional variable $\boldsymbol{z}_{\text{II}}$. The generator of SNGAN-MVP is modified to perform the Hadamard product with respect to the conditional variable every time.

The variants of the generator of Π-Net are described below:

- **Π-Net** (Chrysos et al., 2020): The generator is based on a product of polynomials. The first polynomials use fully-connected connections, while the next few polynomials use cross-correlations. The discriminator is based on the residual blocks of SNGAN. We stress out that the generator does not include any activation functions apart from a hyperbolic tangent in the output space for normalization. The authors advocate that this exhibits the expressivity of the designed model.
- **Π-Net-SICONC**: The generator structure is based on Π-Net with two modifications: a) the Conditional Batch Normalization is converted into batch normalization (Ioffe & Szegedy, 2015), b) the second-input is concatenated with the first (i.e., the noise) in the input of the generator. Thus, this is a single variable polynomial, i.e., a Π-Net, where the second-input is vectorized and concatenated with the first. This baseline implements the Π-Net described in sec. E.
- **MVP** [proposed]: The generator of Π-Net is converted to an MVP model with two modifications: a) the Conditional Batch Normalization is converted into batch normalization (Ioffe & Szegedy, 2015), b) instead of having a Hadamard product with a single variable as in Π-Net, the formula with the two-variable input (e.g., (2)) is followed.
- **GAN-CONC**: Based on MVP, each Hadamard product is replaced by a concatenation. This implements the variant mentioned in sec. D.
- **GAN-ADD**: Based on MVP, each Hadamard product is replaced by an addition. This modifies (14) to $\boldsymbol{x}_n = \left(\boldsymbol{A}_{[n,I]}^T \boldsymbol{z}_{\text{I}} + \boldsymbol{A}_{[n,II]}^T \boldsymbol{z}_{\text{II}}\right) + \left(\boldsymbol{V}_{[n]}^T \boldsymbol{x}_{n-1} + \boldsymbol{B}_{[n]}^T \boldsymbol{b}_{[n]}\right)$.
- **SPADE** (Park et al., 2019): As described in sec. F, SPADE defines a polynomial with respect to the conditional variable $\boldsymbol{z}_{\text{II}}$. The generator of Π-Net is modified to perform the Hadamard product with respect to the conditional variable every time.
- **SPADE-MVP** [proposed]: This is a variant we develop to bridge the gap between SPADE and the proposed MVP. Specifically, we augment the aforementioned SPADE twofold: a) the dense layers in the input space are converted into a polynomial with respect to the variable $\boldsymbol{z}_{\text{I}}$ and b) we also convert the polynomial in the output (i.e., the rightmost polynomial in the Fig. 7 schematics) to a polynomial with respect to the variable $\boldsymbol{z}_{\text{I}}$. This model captures higher-order correlations of the variable $\boldsymbol{z}_{\text{I}}$ that SPADE did not not originally include. This model still includes single variable polynomials, however the input in each polynomial varies and is not only the conditional variable.

The two baselines GAN-CONC and GAN-ADD capture only additive correlations, hence they cannot effectively model complex distributions without activation functions. Nevertheless, they are added as a reference point to emphasize the benefits of higher-order polynomial expansions.

An abstract schematic of the generators that are in the form of products of polynomials is depicted in Fig. 7. Notice that the compared methods from the literature use polynomials of a single variable, while we propose a polynomial with an arbitrary number of inputs (e.g., two-input shown in the schematic).

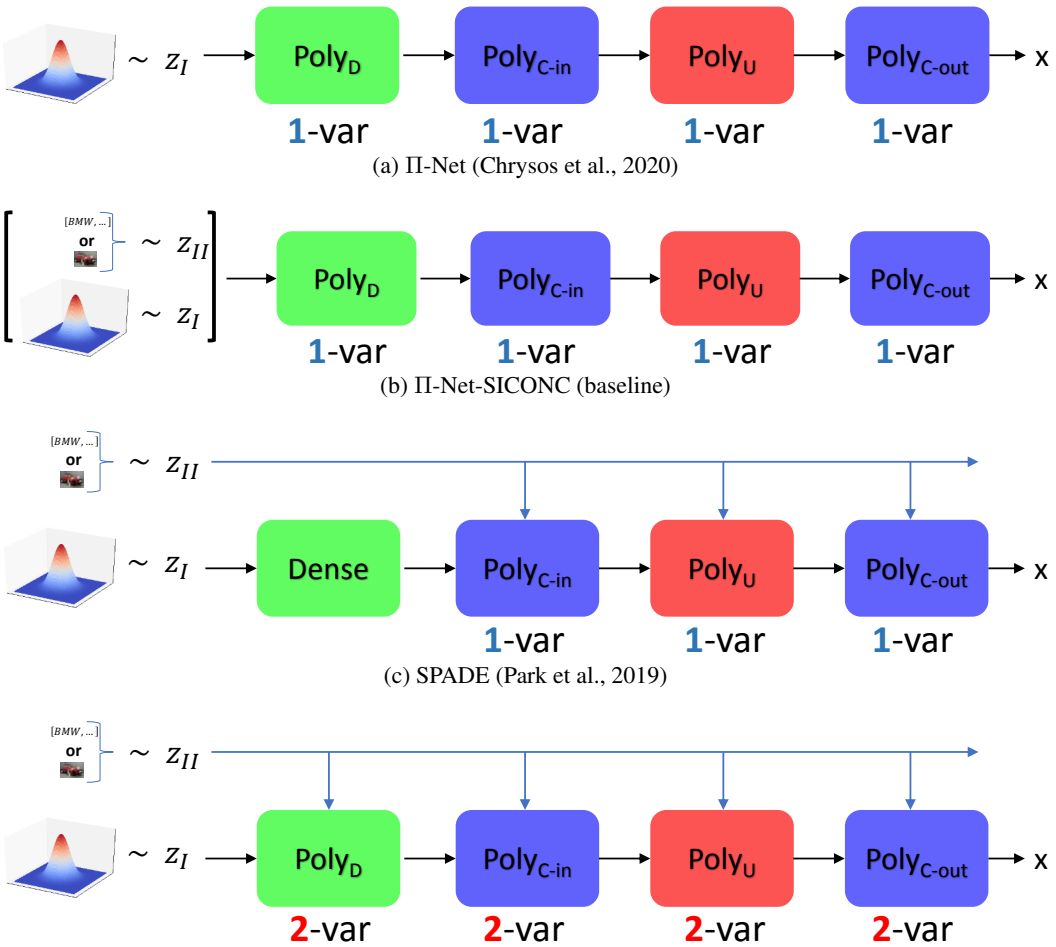

(a) Π-Net (Chrysos et al., 2020)

(b) Π-Net-SICONC (baseline)

(c) SPADE (Park et al., 2019)

(d) MVP (proposed)

Figure 7: Abstract schematic of the different compared generators. All the generators are products of polynomials. Each colored box represents a different type of polynomial, i.e., the green box symbolizes polynomial(s) with dense layers, the blue box denotes convolutional or cross-correlation layers. The red box includes the up-sampling layers. (a) Π-Net implements a single-variable polynomial for modeling functions $\boldsymbol{x} = G(\boldsymbol{z})$. Π-Net enables class-conditional generation by using conditional batch normalization (CBN). (b) An alternative to CBN is to concatenate the conditional variable in the input, as in Π-Net-SICONC. This also enables the non-discrete conditional variables (e.g., low-resolution images) to be concatenated. (c) SPADE implements a single-variable polynomial for conditional image generation. The polynomial is built with respect to the conditional variable $\boldsymbol{z}_{II}$. This is substantially different from the polynomial with multiple-input variables, i.e., MVP. Two additional differences are that (i) SPADE is motivated as a spatially-adaptive method (i.e., for continuous conditional variables), while MVP can be used both for discrete and for continuous type variables, (ii) there is no polynomial in the dense layers in the SPADE. However, as illustrated in Π-Net converting the dense layers into a higher-order polynomial can further boost the performance. (d) The proposed generator structure.

Implementation details of MVP: Throughout this work, we reserve the symbol $\boldsymbol{z}_{\text{II}}$ for the conditional input (e.g., a class label). In each polynomial, we reduce further the parameters by using the same embedding for the conditional variables. That is expressed as:

$$\boldsymbol{U}_{[n,II]} = \boldsymbol{U}_{[1,II]} \tag{19}$$

for $n = 2, \ldots, N$. Equivalently, that would be $\boldsymbol{A}_{[n,II]} = \boldsymbol{A}_{[1,II]}$ in (14). Additionally, Nested-MVP performed better in our preliminary experiments, thus we use (14) to design each polynomial. Given the aforementioned sharing, the Nth order expansion is described by:

$$\boldsymbol{x}_n = \left(\boldsymbol{A}^T_{[n,I]}\boldsymbol{z}_{\text{I}} + \boldsymbol{A}^T_{[1,II]}\boldsymbol{z}_{\text{II}}\right) * \left(\boldsymbol{V}^T_{[n]}\boldsymbol{x}_{n-1} + \boldsymbol{B}^T_{[n]}\boldsymbol{b}_{[n]}\right) \tag{20}$$

for $n = 2, \ldots, N$. Lastly, the factor $\boldsymbol{A}_{[1,II]}$ is a convolutional layer in the case of continuous conditional input, while it is a fully-connected layer in the case of discrete conditional input.

H Additional experiments

Additional experiments and visualizations are provided in this section. Additional visualizations for class-conditional generation are provided in sec. H.1. An experiment with mixed conditional input is conducted in sec. H.4. Additional experiments with class-conditional generation with SVHN digits and translation of MNIST to SVHN digits are conducted in sec. H.2 and sec. H.3 respectively.

H.1 Additional visualizations in class-conditional generation

In Fig. 8 the qualitative results of the compared methods in class-conditional generation on CIFAR10 are shared. Both the generator of SNGAN and ours have activation functions in this experiment.

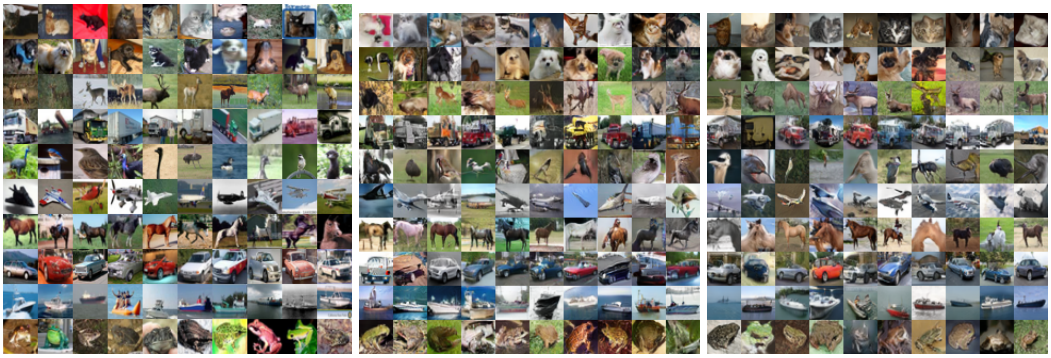

(a) Ground-truth samples (b) SNGAN (Miyato et al., 2018) (c) MVP

Figure 8: Qualitative results on CIFAR10. Each row depicts random samples from a single class.

In Fig. 9 samples from the baseline Π-Net (Chrysos et al., 2020) and our method are depicted for the class-conditional generation on CIFAR10. The images have a substantial difference. Similarly, in Fig. 10 a visual comparison between Π-Net and MVP is exhibited in Cars196 dataset. To our knowledge, no framework in the past has demonstrated such expressivity; MVP synthesizes images that approximate the quality of synthesized images from networks with activation functions.

H.2 Class-conditional generation on house digits

An experiment on class-conditional generation with SVHN is conducted below. SVHN images include (substantial) blur or other distortions, which insert noise in the distribution to be learned. In addition, some images contain contain a central digit (i.e., based on which the class is assigned), and partial visibility of other digits. Therefore, the generation of digits of SVHN is challenging for a generator without activation functions between the layers.

Our framework, e.g., equation 14, does not include any activation functions. To verify the expressivity of our framework, we maintain the same setting for this experiment. Particularly, **the generator**

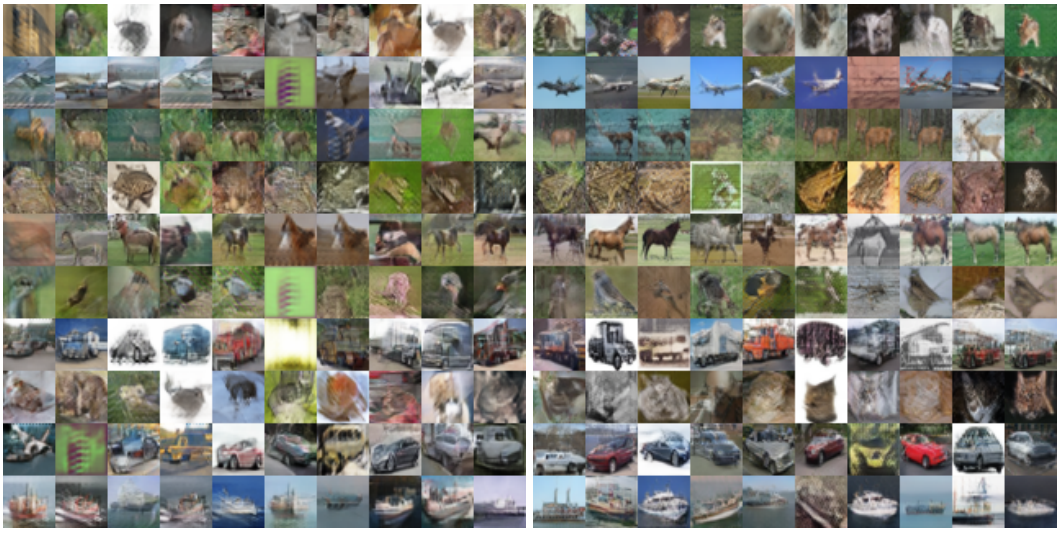

(a) Π-Net (Chrysos et al., 2020) (b) MVP

Figure 9: Qualitative results on CIFAR10 when the generator does not include activation functions between the layers. Each row depicts random samples from a single class; the same class is depicted in each pair of images. For instance, the last row corresponds to boats.

(a) Π-Net (b) MVP

Figure 10: Qualitative results on Cars196 when the generator does not include activation functions between the layers. Each row depicts random samples from a single class; the same class is depicted in each pair of images. The differences between the synthesized images are dramatic.

does not have activation functions between the layers; there is only a hyperbolic tangent in the output space for normalization. The generator receives a noise sample and a class as input, i.e., it is a class-conditional polynomial generator.

The results in Fig. 11(b) illustrate that despite the noise, MVP learns the distribution. As mentioned in the main paper, our formulation enables both inter-class and intra-class interpolations naturally. In the inter-class interpolation the noise $\boldsymbol{z}_{\mathrm{I}}$ is fixed, while the class $\boldsymbol{z}_{\mathrm{II}}$ is interpolated. In Fig. 11(d) several inter-class interpolations are visualized. The visualization exhibits that our framework is able to synthesize realistic images even with inter-class interpolations.

(a) Ground-truth samples (b) MVP (c) Intra-class interpolation (d) Inter-class interpolation

Figure 11: Synthesized images by MVP in the class-conditional SVHN: (a) Ground-truth samples, (b) Random samples where each row depicts the same class, (c) Intra-class linear interpolation from a source (leftmost image) to the target (rightmost image), (d) inter-class linear interpolation. In inter-class interpolation, the class labels of the leftmost and rightmost images are one-hot vectors, while the rest are interpolated in-between; the resulting images are visualized. In all three cases ((b)-(d)), MVP synthesizes realistic images.

H.3 Translation of MNIST digits to SVHN digits

An experiment on image translation from the domain of binary digits to house numbers is conducted below. The images of MNIST are used as the source domain (i.e., the conditional variable $\boldsymbol{z}_{\text{II}}$), while the images of SVHN are used as the target domain. The correspondence of the source to the target domain is assumed to be many-to-many, i.e., each MNIST digit can synthesize multiple SVHN images. No additional loss is used, the setting of continuous conditional input from sec. 4.2 is used.

The images in Fig. 12 illustrate that MVP can translate MNIST digits into SVHN digits. Additionally, for each source digit, there is a significant variation in the synthesized images.

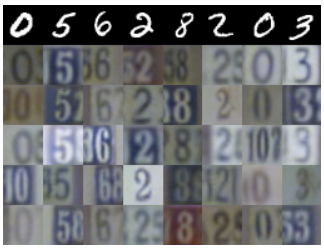

Figure 12: Qualitative results on MNIST-to-SVHN translation. The first row depicts the conditional input (i.e., a MNIST digit). The rows 2-6 depict outputs of the MVP when a noise vector is sampled per row. Notice that for each source digit, there is a significant variation in the synthesized images.

H.4 Multiple conditional inputs

Frequently, more than one type of input conditional inputs are available. Our formulation can be extended beyond two input variables (sec. C); we experimentally verify this case. We select the case of two conditional input variables: one discrete (class label) and one continuous (low-resolution image). Thus, the task is class-conditional super-resolution. We use the experimental details of sec. 4.2 in super-resolution $8\times$. In Fig. 13, we visualize how for each low-resolution image the results differ depending on the randomly sampled class label. The FID in this case is 53.63, which is similar to the previous two cases. Class-conditional super-resolution (or similar tasks with multiple conditional inputs) can be of interest to the community and MVP results in high-dimensional images with large variance.

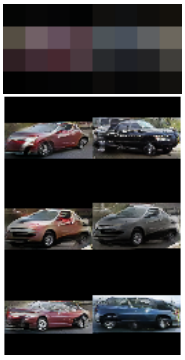

Figure 13: Three-variable input generative model.